Studying 3D Spherical Shell Convection using ASPECT

Grant T. Euen

Thesis submitted to the Faculty of the
Virginia Polytechnic Institute and State University
in partial fulfillment of the requirements for the degree of

Master of Science
in
Geosciences

Scott D. King, Chair
D. Sarah Stamps
Robert J. Weiss

December 6, 2017
Blacksburg, Virginia

Keywords: Mantle Convection, Planetary Science, Code

Studying 3D Spherical Shell Convection using ASPECT

Grant T. Euen

(ABSTRACT)

ASPECT is a new convection code that uses more modern and advanced solver methods than geodynamics legacy codes. I use ASPECT to calculate 2-dimensional Cartesian as well as 2- and 3-dimensional spherical-shell convection cases. All cases use the Boussinesq approximation. The 2D cases come from Blankenbach et al. [2], van Keken et al. [31], and Davies et al. (in preparation). Results for 2D cases agree well with their respective benchmark papers. The time-evolutions of the root mean square velocity (V_{RMS}) and Nusselt number agree, often to within 1%. The 3D cases come from Zhong et al. [35]. Modifications were made to the simple.cc and harmonic_perturbation.cc files in the ASPECT code in order to reproduce the initial conditions and temperature-dependence of the rheology used in the benchmark. Cases are compared using both CitcomS and ASPECT with different levels of grid spacing, as well as comparing uniform grid spacing and the ASPECT default grid spacing, which refines toward the center. Results for V_{RMS}, average temperature, and Nusselt numbers at the top and bottom of the shell range from better than 1% agreement between CitcomS and ASPECT for cases with tetragonal planforms and 7000 Rayleigh number to as much as 44% difference for cases with cubic planforms and 10^5 Rayleigh number. For all benchmarks, the top Nusselt number from ASPECT is farthest from the reported benchmark values. The 3D planform and radially averaged quantity plots agree. I present these results, as well as recommendations and possible fixes for discrepancies in the results, specifically in the Nusselt numbers, V_{RMS}, and average temperature.

Studying 3D Spherical Shell Convection using ASPECT

Grant T. Euen

(GENERAL AUDIENCE ABSTRACT)

Mantle convection is the primary process in which heat is transferred from the interior of Earth to its exterior. It is a process that involves the physical movement of material in the mantle: hot material rises towards the surface and cools, while cold material sinks to the base and warms. This transferring of heat and energy is also the driving force behind plate tectonics, the process in which the surface of the Earth moves and changes with time. Plate tectonics is responsible for the formation of oceans, mountains, volcanoes, and trenches to name a few. Understanding the behavior of the mantle as it convects is crucial to understanding how the Earth and planetary bodies like it develop over time. In this work, I use the new modeling code ASPECT, Advanced Solver for Problems in Earths ConvecTion, to test various models in 2 and 3 dimensions. This is done to compare the results calculated by ASPECT with those of older, legacy codes for the purpose of benchmarking and growth of ASPECT. Insight is also gleaned into the large-scale factors that influence mantle convection and planetary development. My results show good agreement between results calculated by ASPECT and those of legacy codes, though there is some discrepancy in some values. The main values I present here are V_{RMS}, the root mean square velocity, the average temperature, and the Nusselt number calculated for both the top and base of the models. In this work, I present these results and potential solutions to the discrepancies encountered.

Contents

List of Figures

List of Tables

Chapter 1

Introduction

The theory of plate tectonics gained a strong scientific following during the 1960s, though the argument can be made that the idea has been evolving for far longer [1, 11, 20, 24]. Although it was a point of vigorous debate for decades, today it is widely accepted by scientists all over the world. In spite of this acceptance the true behavior of the Earths mantle is still not fully understood. Work continues to link the physical events and characteristics we see on the surface to the internal workings of the mantle. These characteristics include mid-oceanic ridges, mountain ranges, volcanoes, hot spots, and oceanic trenches. Collecting data for these characteristics pose a difficult challenge, as the motions and events described occur on a planetary scale, and are often located in remote or dangerous parts of the world. Also, unlike the effects on the surface that we as scientists can directly observe, the motions of the mantle must be indirectly inferred, adding to the obscurity to an already challenging problem. Still, this study is vastly important. Understanding mantle convection tells us how our planet behaves throughout time [25]. The formation and destruction of oceans, the movement of continents, and the heat budget of the Earth itself all relate back to mantle convection [1, 24]. As its past behaviors are understood, predictions can be made about the future behaviors of our planet as well. Fully understanding mantle convection in Earth's mantle can also have implications outside of our planet. As more is learned about the other bodies in our Solar System, and exoplanets beyond it, understanding the role that mantle convection plays in surface features and geologic phenomena becomes that much

more important.

The main piece of evidence we know for mantle convection is continental drift, known now as plate tectonics [1]. The motions of the Earths surface that we can now detect and measure are attributed to the motions of several large, rigid plates, as well as a few microplates [6]. All of these plates are in motion; often the motions are recorded in frames of reference with one plate or feature held constant and the relative motions of everything else measured [30]. Once this motion became widely accepted, its driving force was quickly agreed upon [8, 29]. Heat escaping from the interior of Earth was causing materials to increase in temperature over millions of years. These hotter materials also experienced a decrease in density, and therefore became unstable. They began rising towards the surface, while simultaneously colder material that had been near the surface for millions of years, cooled off, increased in density, and began sinking towards Earths interior. The heated material would rise higher, give off its excess heat, and sink back down again, while the cooled material would sink, gain excess heat, and begin rising back to the surface. This physical circulation driving heat out of the interior towards the surface is what we know as mantle convection, and sections where hot material rises up causes plates to move apart, while sections where cold material subducts brings plates together. The areas where plates are pushed apart typically cause massive lowlands to be formed, though there are large ridges at the centers of these systems. There are notable exceptions, one of the most important being the East African Rift System. This area is rifting apart, however there is uplift in the entire region. On Earth these massive lowland areas fill with water and eventually become oceans. The term seafloor spreading was coined by Dietz [7], as oceans are pushed ever wider at roughly the center of their abyssal plains. Hot mantle rock flows to fill in the gap left by the spreading plates. This material accretes onto the base of the plates. This causes the plates to thicken and become denser, which causes them to sink into the underlying mantle. This difference of hot, thin material

at the ridge and cooler, thicker material to either side causes a gravitational body force which causes older material to be pushed away from these mid-oceanic ridges [30]. This process is often mostly symmetric. Areas where plates are pushed together cause localized, but more extreme effects. If two continental plates meet large highlands, mountain ranges, will form. If at least one of the plates is oceanic, extreme lowlands will form. These are the oceanic trenches, the deepest parts of Earths surface. Colder material sinks down at these trenches and dives back into the Earths interior to be reheated and rise again. Unlike seafloor spreading, this process of subduction is always completely asymmetric, as only one plate subducts.

These two physical systems, tectonic plates and mantle convection, are coupled which has been a major point of study: which system drives the processes [1]? The fact that subduction of plates occurs at areas of downwelling of cold material in the mantle, means that the mantle convection will have to follow the structure of the overlying tectonic plates. These plates are rigid and much colder than the mantle, which means they can penetrate into the mantle once they subduct. Because they are cold and dense, they are the antithesis of hot material upwelling from the base of the mantle. This is to say, the convection of the mantle is primarily on the scale of the tectonic plates and the pattern of convection is closely related to how the plates are oriented to each other [1]. There are arguments for cases of small-scale convection as well, where small convective cells in the first few hundred kilometers of the upper mantle form [14, 23]. These small-scale cells are one potential explanation for intraplate volcanism. Due to the higher strength of the lithosphere, the flow pattern of the mantle is determined by the geometry of the plates. Studies have been done to show this coupling. Numerical models from Davies [4] and Davies [5] were compared to show that convection in a uniform medium, that is, constant viscosity throughout, develops a convection pattern that is different than a model that includes a strong upper boundary layer. In the uniform viscosity case, the

pattern that developed was largely equal sized convection cells throughout the medium. In the case with the strong boundary layer, created by imposing a temperature dependence on the viscosity, low viscosity faults were added to the boundary layer to allow points for flow to commence [33]. As expected, the flow pattern that emerged in this case was dictated by the boundaries of these faults in the higher viscosity boundary. However, this is only a first-order behavior. The flow of convection in the mantle has more complexities to it; however, these complexities are on smaller scales than the tectonic plates [1]. In the Earth's mantle viscosity is not uniform. The viscosity of a fluid is based primarily on the temperature of the fluid, and the pressure the fluid is under [30]. These factors will cause different flow. For example, honey at room temperature will be much more viscous than honey heated to twice that. However, overall composition of the fluid can also have an effect. For example, water heated to the same temperature as the heated honey will also flow differently. The mantle is made of rigid material that is under great pressure that increases with depth. It is also heated from below, and is therefore hotter with depth, as well as being heated internally by radioactive decay. The composition of the mantle is also not fully known, and a change in composition with depth could cause breaks in flow [30]. Convective flow of the mantle is a very complex process over a planet-wide scale. This makes its study a challenge.

In order to try to understand something so large scale that we cannot directly observe it, computer codes have been developed [15, 28, 34]. These legacy codes, such as ConMan and CitcomS, utilize equations of fluid mechanics and quantities derived from observation and evidence left over on the surface of the Earth to solve huge systems of equations with potentially millions of unknowns. For instance, in section 5.2.1 in the ASPECT manual a 2D convection box problem, which will be discussed in detail in section 3.1 of this work, is described at 4 different levels of initial global refinement. From coarsest mesh to finest mesh, the number of unknowns being solved for increases from on the order of 1000 to 100000. In

3D cases, the increase between refinement levels is larger. These codes generate numbers, images, and behaviors that are used to develop models to better explain and understand mantle convection. They have been used to calculate convective flow models in both the Cartesian and spherical domains, as well as take more complex constraints into account. As time has gone on, codes have incorporated phase transitions, chemical heterogeneities, and varying viscosity behavioral laws [3, 9, 13, 27]. Many of these codes have been around and utilized for decades; however, as time moves forward technology improves, and codes and the computers that run them advance. Newer codes are written that utilize new technologies, new techniques, and new discoveries. As they are completed and begin to be utilized by scientists it is important to ensure that the answers they generate are comparable to previously used codes to be certain they are calculating answers as they should. To that end, there are many well-known problems that have been extensively tested in geodynamics that can be used to compare mantle convection codes [2, 16, 31, 35], especially spherical shell problems using a temperature-dependent viscosity [22, 32, 34, 35].

ASPECT, Advanced Solver for Problems in the Earths ConvecTion, is a geodynamics code that has been around for less than a decade [17] and uses newer solving techniques to tackle modeling of mantle convection. The main innovations that ASPECT utilizes are how it is built and its grid. ASPECT is an open source code that is built on several other open source packages. It utilizes massive databases like Trilinos and deal.II to do its calculations. ASPECT uses biquadratic solver elements in contrast to the linear elements used by legacy codes. ASPECT also uses adaptive mesh refinement to attempt to make calculations as efficient as possible, refining grids where more detail is needed and coarsening it where it is not. Cells in need of refinement will be split into 4 daughter cells in 2D or 8 daughter cells in 3D. ASPECT takes advantage of P4EST for distributed, adaptive meshes. I test ASPECT using a number of known cases in both 2 and 3 dimensions and compare its results with

known answers generated by the legacy convection codes ConMan and CitcomS. The tests come from several different papers and are included as cookbook tests in ASPECT. 2D tests come from Blankenbach et al. [2] and van Keken et al. [31]. A 2.5D or 2D spherical case, used here as a midway point between 2D and 3D behavior, comes from a paper by Davies et al. (in preparation). 3D cases all come from Zhong et al. [35] and are variations on its "A family" and "C family" of tests. This will be gone into more deeply in Section 3.

Chapter 2

Equations of Motion

The equations of motion governing mantle convection are the conservation of mass, momentum, and energy [10]. These are given by

$$0 = \frac{\partial \rho}{\partial t} + \nabla \cdot (\rho \vec{v}) = \frac{D\rho}{Dt}, \tag{2.1}$$

$$\rho \left[\frac{\partial \vec{v}}{\partial t} + \vec{v} \cdot \nabla \vec{v} \right] = -\nabla P + \rho \vec{g} + \frac{\partial \tau_{ij}}{\partial x_j}, \tag{2.2}$$

and

$$\rho \frac{Dq}{Dt} = \nabla \cdot (k \nabla T) + \rho H + \tau_{ij} \frac{\partial v_i}{\partial x_j}, \tag{2.3}$$

where $\frac{D}{Dt} = \frac{\partial}{\partial t} + \vec{v}$ is the material derivative, ρ is density, t is time, $\vec{v}$ is velocity, P is pressure, $\vec{g}$ is gravity, τ_{ij} is the deviatoric stress tensor, k is thermal conductivity, T is temperature, and H is the rate of heat generation.

Using the thermodynamic relations

$$dq = TdS \tag{2.4}$$

and

$$dS = \frac{c_P}{T} dT - \frac{\alpha}{\rho} dP, \tag{2.5}$$

Equation 2.3 can be rewritten as

$$\rho c_P \frac{DT}{Dt} - \alpha T \frac{DP}{Dt} = \nabla \cdot (k \nabla T) + \rho H + \phi \tag{2.6}$$

where ϕ is the viscous dissipation given by

$$\phi = \eta \left[(\nabla \vec{v} + \nabla \vec{v}^T) - \frac{2}{3} \nabla \cdot \vec{v} \right] + \eta_b \nabla \cdot \vec{v}, \tag{2.7}$$

where η is the dynamic 'shear' viscosity and η_b is the bulk viscosity.

We can set $\frac{\partial \rho}{\partial t} = 0$ because flow velocities in the mantle are much lower than the velocity of sound. We can also set the right hand side of Equation 2.2 to zero because the Prandtl number is large. Thus

$$0 = \nabla \cdot (\rho \vec{v}) \tag{2.8}$$

and

$$0 = -\nabla P + \rho \vec{g} + \nabla \left[\eta \left[(\nabla \vec{v} + \nabla \vec{v}^T) - \frac{2}{3} \nabla \cdot \vec{v} \right] \right]. \tag{2.9}$$

To compare Equation 2.6, with the equations in the ASPECT manual, I further write the total derivative of pressure with respect to time into its time component and flux along the

flow component,

$$\rho c_P \left[\frac{\partial T}{\partial t} + \vec{v} \cdot \nabla T\right] - \alpha T \left[\frac{\partial P}{\partial t} + \vec{v} \cdot \nabla p\right] = \nabla \cdot (k \nabla T) + \rho H + \phi. \tag{2.10}$$

Comparing Equation 2.10 here with Equation 3 in the ASPECT manual, page 9, the only difference is that the authors of ASPECT have assumed that $\frac{\partial P}{\partial t} = 0$. Legacy codes also make this assumption [16]. The last term in the ASPECT manual, Equation 3, is the latent heat associated with phase transformations. This is also included in legacy codes, but not part of the work here. In addition, in the work here we will not be considering internal heating, H, or viscous dissipation, ϕ.

2.1 ASPECT

Here I describe how ASPECT differs from legacy codes. There are no differences in the assumed laws of physics or approximations. Most previous codes were modified from an incompressible limit and start from the assumption that the equation of state, $\rho = f(P, T)$, can be linearized about a reference state. This allows fewer assumptions to the magnitude of density variations; however, it comes at the price of being difficult to construct a model with an *a priori* density structure.

It has been standard practice in geodynamics to solve Equations 2.1 and 2.2 starting from a reference density, and therefore reference pressure, profile *a priori*. In the appendix of Kronbichler et al. [17], they show that it requires the same number of iterations to calculate the absolute pressure as it does to calculate the deviatoric pressure. In their methodology, there is no loss in performance for calculating the full density and pressure. The greater use of 64-bit arithmetic also allows this to be possible. In many older convection codes,

breaking the pressure and density into a reference and deviatoric term gave some numerical advantages and allowed some further simplifications.

Below is the derivation of splitting the pressure and density into a reference state and a perturbation from that state. The reference profile is fixed throughout the calculation. Introducing the expansions

$$P = P_r + P' \tag{2.11}$$

and

$$\rho = \rho_r(P_r) + \rho'(P', T), \tag{2.12}$$

where the subscript r denotes the reference value of the property it is associated with and the primed variables represent departures from the reference state, the equations for the conservation of mass, momentum and energy become

$$0 = \nabla \cdot [(\rho_r + \rho') \cdot \vec{v}], \tag{2.13}$$

$$0 = -\nabla P_r - \nabla P' + \rho_r \vec{g} + \rho' \vec{g} + \nabla \left[\eta \left[(\nabla \vec{v} + \nabla \vec{v}^T) - \frac{2}{3} \nabla \cdot \vec{v} \right] \right], \tag{2.14}$$

and

$$\rho c_P \frac{DT}{Dt} - \alpha T[\vec{v} \cdot \nabla P_r + \vec{v} \cdot \nabla P'] = \nabla \cdot (k \nabla T) + \rho H + \phi, \tag{2.15}$$

respectively.

The value of P_r is time independent and spatially variable only in the vertical direction, i.e.,

$$\nabla P_r = \frac{\partial P_r}{\partial z}\vec{e}_z = \rho_r \vec{g}. \tag{2.16}$$

Thus Equations 2.14 and 2.15 become

$$\nabla P' = \rho' \vec{g} + \nabla \left[\eta \left[(\nabla \vec{v} + \nabla \vec{v}^T) - \frac{2}{3} \nabla \cdot \vec{v} \right] \right] \tag{2.17}$$

and

$$\rho c_P \frac{DT}{Dt} - \alpha T [\vec{v} \cdot P' + \vec{v} \cdot (\rho_r \vec{g})] = \nabla \cdot (k \nabla T) + \rho H + \phi. \tag{2.18}$$

Notice that the momentum equation, Equation 2.17, now depends only on departures from the reference pressure and density profiles. Dividing the variables by the normalization factors, the non-dimensional forms of the mass, momentum and energy equations becomes

$$\nabla \cdot ((\rho_r + \rho')\vec{v}) = 0, \tag{2.19}$$

$$\nabla P' = Ra \rho' \vec{e}_z + \nabla \left[\eta \left[(\nabla \vec{v} + \nabla \vec{v}^T) - \frac{2}{3} \nabla \cdot \vec{v} \right] \right], \tag{2.20}$$

and

$$\rho c_P \frac{DT}{Dt} - \alpha T Di \left(\frac{\alpha_o \Delta T}{Ra} \vec{v} \cdot \nabla P' + \rho_r \vec{v} \cdot \vec{e}_z \right) = \nabla \cdot (k \nabla T) + \rho H + \frac{Di}{Ra} \phi, \tag{2.21}$$

where

$$Ra \equiv \frac{\rho_o g_o \alpha_o \Delta T h^3}{\eta_o \kappa_o} \tag{2.22}$$

and

$$Di \equiv \frac{\alpha_o g_o h}{c_{Po}}. \tag{2.23}$$

The present form of the equations of mass, momentum, and energy is known as the anelastic liquid approximation (ALA). Upon careful reading of Jarvis and McKenzie [10] one might make the case that the ALA also makes the specific additional assumption that the effect of pressure and temperature on ρ' is linear and drop the effect of ρ' in Equations 2.19 and 2.20.

$$\rho(P,T) = \rho_r(1 - \alpha(T - T_r) + K_T^{-1}(P - P_r)) \tag{2.24}$$

where

$$\alpha = \rho_r^{-1} \left(\frac{\partial \rho_r}{\partial T} \right)_P \tag{2.25}$$

and

$$K_T = \rho_r \left(\frac{\partial P}{\partial \rho_r} \right)_T. \tag{2.26}$$

2.2 Boussinesq Formulation

In the benchmarks considered here [2, 35], the Boussinesq formulation is used. The Boussinesq formulation assumes that the density is constant everywhere except for the buoyancy term and that the dissipation number is zero. This is the only term where density appears that is not a derivative. With the Boussinesq approximation, Equations 2.19-2.21 reduce to

$$0 = \nabla \cdot \vec{v} \tag{2.27}$$

$$0 = -\nabla P + Ra\vec{g} + \nabla \left[\eta(\nabla\vec{v} + \nabla\vec{v}^T)\right], \tag{2.28}$$

and

$$\rho c_P \left[\frac{\partial T}{\partial t} + \vec{v} \cdot \nabla T\right] = \nabla \cdot (k\nabla T). \tag{2.29}$$

The challenge using ASPECT for a Boussinesq problem is that in ASPECT, density, ρ, is variable everywhere. If one assumes density is constant, then there is no driving buoyancy force and if one assumes that density varies with temperature, then Equation 2.19 does not reduce to 2.27, and the $\Delta \cdot \vec{v}$ term in 2.20 does not vanish.

The ASPECT manual suggests one solution. If all the variables in the problem are set to '1', and α is set to a small value and the value of g is set to the Rayleigh number divided by α, then Equation 2.20 approximates 2.28 and density in 2.19 and 2.21 becomes almost constant. This is one approach that is used to solve the problems in this work. In addition, over the course of this work, the developers implemented a Boussinesq formulation. This is used for most of the work in this thesis.

Chapter 3

Results

In this section I describe my efforts to compare ASPECT with a set of 3D spherical calculations described in Zhong et al. [35]; also called the Zhong benchmark. Here, I first describe my comparison with other 2D mantle convection benchmarks.

3.1 2D Boussinesq Case: Convection Box in Blankenbach et al. [2]

To test if my installation of ASPECT functions properly, and that I use it correctly, I perform tests in 2D Cartesian geometry. These tests require less computing time than the corresponding 3D cases, and there are a number of published benchmark papers that compare the results from these cases with a number of convection codes. Several of these tests are described in the ASPECT manual and the results match published values better than the initial cases I ran in 3D. I document my 2D Cartesian results here to illustrate the performance of ASPECT with known solutions. I analyze both the full-scale time-series as well as small-scale perturbations in the time-series near steady state, which I will go into in more detail.

I begin with a well-known problem in computational geophysics, consisting of 2D thermal convection of a non-rotating, constant-property, Boussinesq fluid with infinite Prandtl num-

ber in a rectangular, closed cell [2]. The parameters are described and reproduced in Table 3.1 below. The domain is a square box of dimensions $[0, 1] \times [0, 1]$, heated from below, insulated on the left and right sides, and cooled from the top. The temperature is fixed to 0 at the top and 1 at the bottom, with no internal heat sources. Boundary conditions for velocity are set to allow tangential flow along all four sides of the box, i.e., free slip boundary conditions. The problem can be described by a single parameter, the Rayleigh number,

$$Ra = \frac{\alpha g \Delta T D^3}{\kappa \nu}, \tag{3.1}$$

where α is the coefficient of thermal expansion, g is gravity, ΔT is the change in temperature across the domain, D is the depth of the domain, κ is the thermal diffusivity, and ν is the kinematic viscosity. For the three cases, the Rayleigh number is set to 10^4 (case 1a), 10^5 (case 1b), and 10^6 (case 1c). The problem is run to steady-state. For each code described in the paper, values were reported for the Nusselt number, a ratio of the average surface heat flow from the convective solution to the heat flow due to conduction,

$$Nu = -\frac{\kappa \int_0^1 \frac{\partial T(x,z=1)}{\partial x} dx}{\kappa \Delta(\frac{T}{D})}, \tag{3.2}$$

where the non-dimensional coordinate z is defined to be 1.0 at the surface of the domain, ΔT is the temperature contrast across the domain, and D is the depth of the box. Blankenbach et al. [2] also reports the non-dimensional root mean square velocity,

$$V_{RMS} = \left[\int_0^1 \int_0^1 (u^2 + w^2) dx \;\; dz \right]^{\frac{1}{2}}, \tag{3.3}$$

where u is the horizontal component of velocity and w is the vertical component of velocity. While other measures of the solution are reported in Blankenbach et al. [2], these are the ones most commonly referenced.

Table 3.1: Parameters used in Blankenbach et al. [2] experiments.

Parameter	Symbol	Value
depth of fluid	D	10^6 m
density	ρ	4×10^3 kg/m^3
temperature difference	ΔT	1000 K
thermal diffusivity	κ	10^{-6} m^2 s^{-1}
thermal expansion coefficient	α	2.5×10^{-5} K^{-1}
gravitational acceleration	g	10 m s^{-1}
viscosity	η_o	10^{23} Pa s for Blankenbach 1a
		10^{22} Pa s for Blankenbach 1b
		10^{21} Pa s for Blankenbach 1c
gravitational constant	G	6.67×10^{-11} N m^2 kg^{-2}

Section 5.2.1 of the ASPECT manual describes benchmark tests from Blankenbach et al. [2]. The authors describe a method using the value of gravity, g, and the thermal expansion coefficient, α, for getting the full density used in ASPECT to approximate the uniform density used in Boussinesq cases while still using constant, non-dimensional values for the remaining parameters. This needs to be done because ASPECT uses the full pressure and density in its equations (see section 2.1). In Blankenbach et al. [2], all values are set to be constants including the reference density. However, the primary equations in ASPECT use the full density, which has a temperature-dependent term, $\rho = \rho_o(1 - \alpha T)$, and is not consistent with the standard Boussinesq approximation used in the geodynamics community [30]. The ASPECT manual suggests using the gravity and thermal expansion coefficient values to counteract each other, and produce the desired Rayleigh number. In the ASPECT formulation the buoyancy term is $\rho_o(1-\alpha T)g$, giving a constant $\rho_o g$ term and an $\alpha g T$ term. One can solve the problem non-dimensionally with $g = Ra$ and all other parameters set to 1.0. However, in the energy equation, the density will be $\rho_o(1 - \alpha T)$ and with $\rho_o = 1$ and $\alpha = 1$ will vary between 0 and 1 depending on the value of T. To make this term approach 1.0, I use a small value of α and in the buoyancy term I use $g = Ra * \frac{1}{\alpha}$. This makes the temperature variation of the full density (i.e., $\rho_o(1 - \alpha T)$) small, effectively making the full

density constant, while also allowing the buoyancy term to be the Rayleigh number. In the manual, the results use a global refinement of 4, however the authors suggest using higher refinements to stabilize the values. I test global refinement 3 through 7 for each case. The results for the case presented in the ASPECT manual (case 1a at 4 global refinements) are in good agreement with the values published in the manual.

The following results are generated using the cookbook convection box case in 2D provided with the ASPECT source code. All parameters are set to a non-dimensional value of 1.0, except for α and g which are used to control the Rayleigh number and density as described above. A value of 10^{-10} is used for α for all cases reported. Values of 10^{14}, 10^{15}, and 10^{16} are used for g in cases 1a/2a, 1b, and 1c, respectively. Results are compared against results generated using the convection code ConMan [12, 15], as well as Christensen's extrapolated values from the Blankenbach benchmark paper [2]. Here I note that ConMan uses bilinear elements for both temperature and velocity and iterates to steady-state using Picard iteration [12, 15] while ASPECT uses biquadratic elements in velocity and temperature. In addition, ConMan uses a direct solver for the Stokes equation. I do not use the adaptive mesh refinement feature of ASPECT for these problems.

My results are in good agreement with published results for ASPECT (Tables 3.2-3.4). Case 1a is the most stable across all global refinements tested in both final steady-state values (Table 3.2) and in time-evolution (Figure 3.1), though values for the V_{RMS} and Nusselt number do not reach the same level of agreement with Christensen's extrapolated value as ConMan for velocity (Table 3.2). Christensen's results use bicubic-spline elements and the results extrapolated from increasingly refined grids are generally taken to be the best approximation for the exact values of the solution. The time-series of the RMS velocity shows the same general trend for all 5 grids. The first peak in the RMS velocity time-series moves closer to the end-state time with increasing grid refinement (Figure 3.1) because with

Table 3.2: Blankenbach et al. [2] Benchmark 1a: Steady State, 2D, constant viscosity convection in a 1 by 1 box with Rayleigh number 10^4.

Code	Grid	Global Refinement	V_{RMS}	Nusselt No.
ConMan	50x50		42.906	4.887
ConMan	100x100		42.875	4.885
ConMan	200x200		42.867	4.885
‡ASPECT	8x8	3	46.038	4.651
‡ASPECT	16x16	4	43.459	4.787
‡‡ASPECT	16x16	4	43.459	4.787
‡ASPECT	32x32	5	42.939	4.879
‡ASPECT	64x64	6	42.876	4.890
‡ASPECT	128x128	7	42.870	4.887
†C_{ext}			42.865	4.884
†Christensen′s extrapolated values. ‡CFL number 1.0, and solver tolerance 10^{-7} ‡‡Case run using the Boussinesq Approximation in ASPECT				

increasing grid refinement ASPECT takes smaller timesteps and the time-evolution is more accurately captured. The RMS velocity time-series for global refinements 5-7 plot nearly on top of one another, showing that not only is the final solution converging to a constant value for these cases, but the time-evolution of the solutions is converging as well.

Because I find in my initial testing that the 3D spherical cases are evolving in time along a different path than the corresponding cases with the code CitcomS [34], I look in detail at the time-evolution of the RMS velocity in the non-dimensional time window 0.4-0.5 (see Figures 3.2). In this time window there is no apparent trend in the time-series (increasing or decreasing) and the oscillations, which cannot be seen in Figure 3.1, are smaller than 0.001% (Figure 3.2).

The results for Case 1b (see Figure 3.3 and Table 3.3) are similar, like in Case 1a. Again, the values for V_{RMS} and Nusselt number did not reach the same level of agreement with Christensen's extrapolated values as ConMan (Table 3.3). The same general trend is seen in the time-series plots of the different 5 grids. There is an initial large spike, followed by

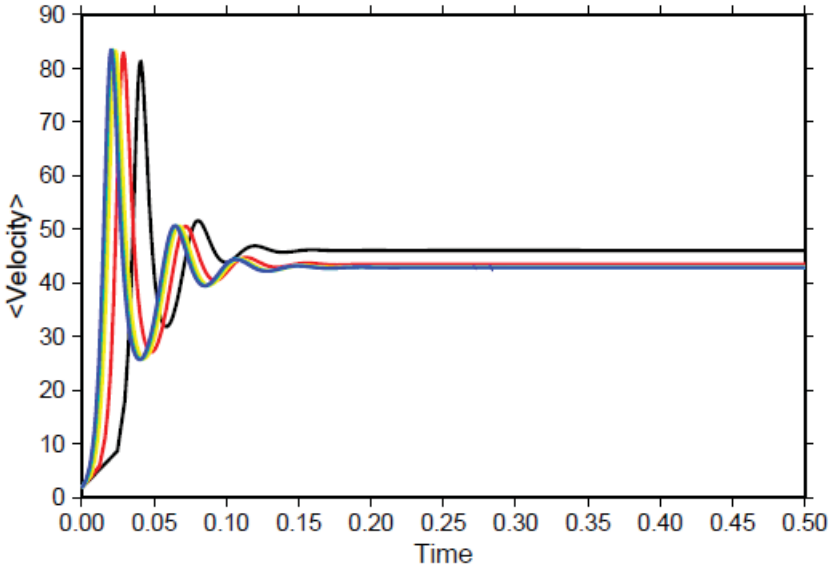

Figure 3.1: Root mean square (RMS) velocities from case 1a of Blankenbach et al. [2] at global refinements 3 (black), 4 (red), 5 (yellow), 6 (green), and 7 (blue).

a damping sinusoidal oscillation to the steady state. The steady state plateaus decrease in value towards Christensen's extrapolated value for the velocity (Figure 3.3). Once again, the time-series for global refinements 5-7 plot nearly consistent with one another showing a convergence of behavior of the entire test case. I note that here the behavior of 3 global refinements behaves differently from the other cases. The large mesh, in this case 8x8 biquadratic elements, is not sufficient to resolve the solution for the higher Rayleigh number cases. This behavior is even more pronounced for cases 1c and 2a.

Similarly to the 1a cases, the time-evolution of the RMS velocity in the non-dimensional time window 0.4-0.5 shows no apparent trend in the time-series (increasing or decreasing) and the oscillations, which cannot be seen in Figure 3.3, are smaller than 0.0001%.

Case 1c (Figure 3.4) is not as well-behaved as the previous cases in that there are significant jumps in the V_{RMS} and temperature values as the grid is refined (Table 3.4). At 3 global refinements the values differ from the best result by a factor of 2, and 4 global refinements

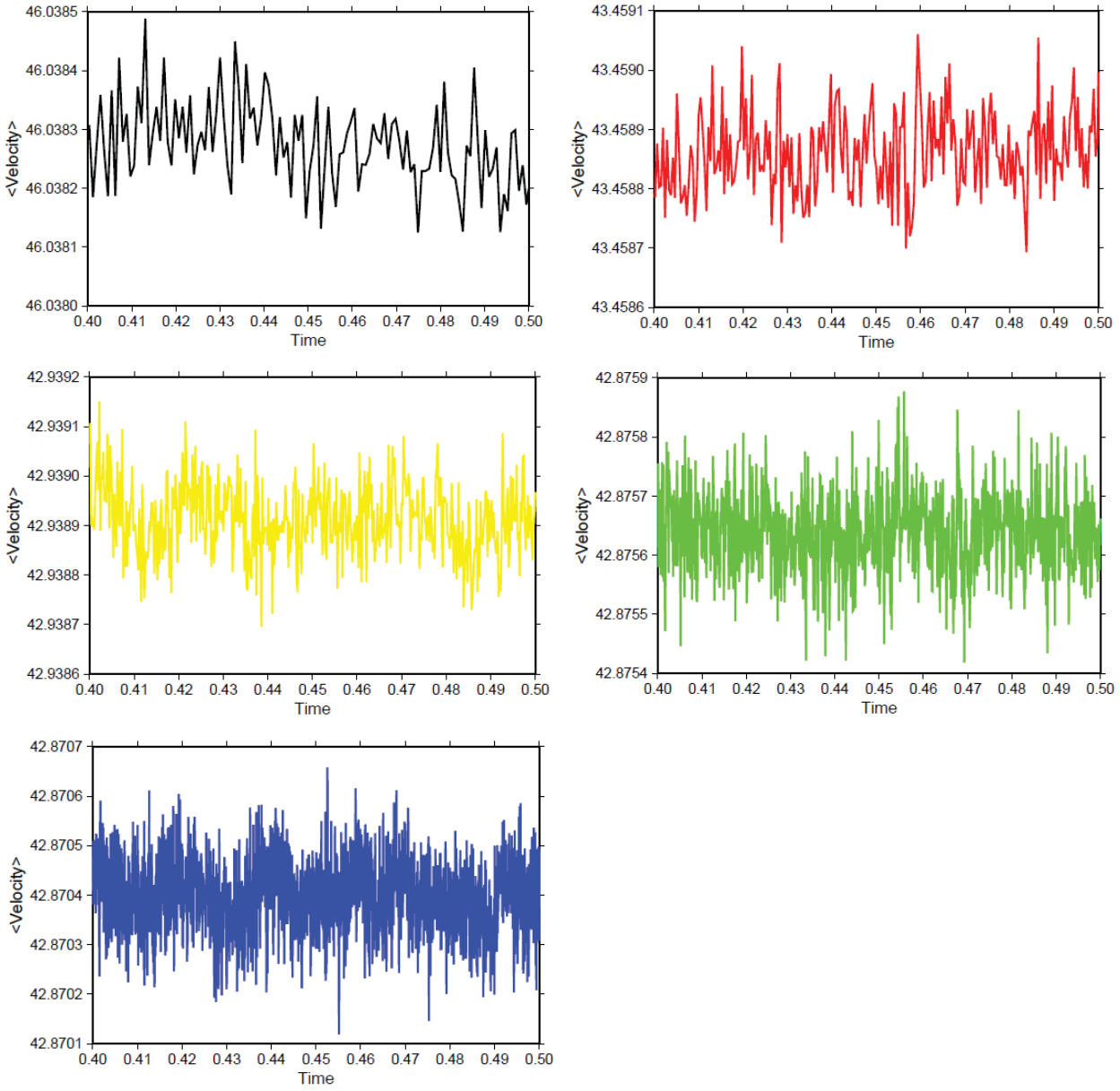

Figure 3.2: Small-scale oscillations for Blankenbach et al. [2] case 1a at global refinement 3 (black), 4 (red), 5 (yellow), 6 (green), and 7 (blue). Plots are zoomed in to the final portion of the runs, time 0.4 to 0.5. Oscillations are all smaller than 0.001%.

Table 3.3: Blankenbach et al. [2] Benchmark 1b: Steady State, 2D, constant viscosity convection in a 1 by 1 box with Rayleigh number 10^5.

Code	Grid	Global Refinement	V_{RMS}	Nusselt No.
ConMan	50x50		193.592	10.546
ConMan	100x100		193.297	10.539
ConMan	200x100		193.248	10.536
‡ASPECT	8x8	3	239.088	8.701
‡ASPECT	16x16	4	209.675	10.114
‡ASPECT	32x32	5	196.525	10.291
‡ASPECT	64x64	6	193.656	10.516
‡ASPECT	128x128	7	193.311	10.549
†C_{ext}			193.214	10.534
†Christensen's extrapolated values. ‡CFL number 1.0, and solver tolerance 10^{-7}				

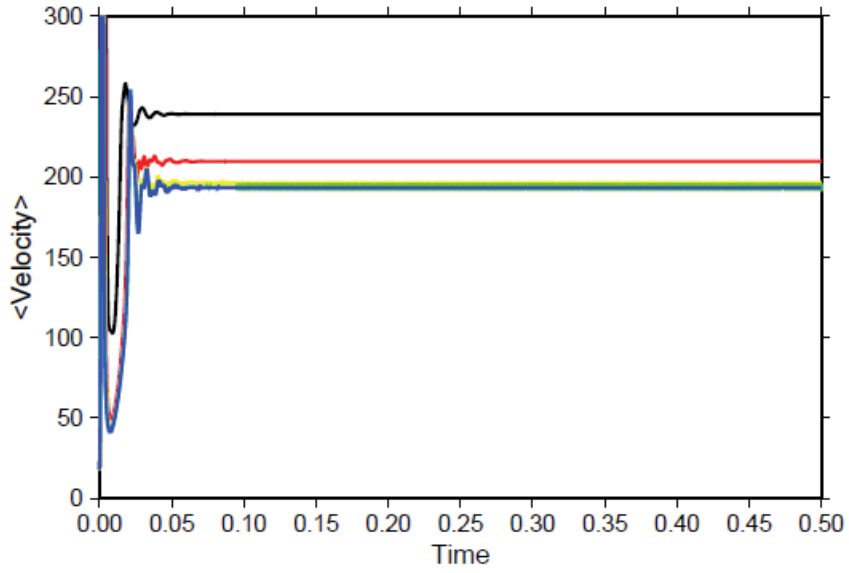

Figure 3.3: Root mean square (RMS) velocities from case 1b of Blankenbach et al. [2] at global refinements 3 (black), 4 (red), 5 (yellow), 6 (green), and 7 (blue).

Table 3.4: Blankenbach et al. [2] Benchmark 1c: Steady State, 2D, constant viscosity convection in a 1 by 1 box with Rayleigh number 10^6.

Code	Grid	Global Refinement	V_{RMS}	Nusselt No.
ConMan	50x50		840.524	21.864
ConMan	100x100		835.606	22.023
ConMan	200x200		834.353	21.981
‡ASPECT	8x8	3	1827.714	9.053
‡ASPECT	16x16	4	482.094	16.613
‡ASPECT	32x32	5	902.945	21.122
‡ASPECT	64x64	6	849.695	21.333
‡ASPECT	128x128	7	835.589	21.881
†C_{ext}			833.989	21.997
†Christensen′s extrapolated values. ‡CFL number 1.0, and solver tolerance 10^{-7}				

still shows a 40% and 25% discrepancy in the steady values of V_{RMS} and Nusselt number, respectively. Global refinements 5, 6, and 7 approach Christensen's extrapolated values.

Again, similarly to the 1a cases, the time-evolution of the RMS velocity in the non-dimensional time window 0.4-0.5 also has no apparent trend in the time-series (increasing or decreasing) and the oscillations, which cannot be seen in Figure 3.4, are smaller than 0.0001%.

Here I describe the set-up for Case 2a. The material model simpler.cc had to be modified to match the rheology used in Blankenbach et al. [2]. This material model is used for simple, cookbook problems that do not require complex parameters or flow laws. It was implemented by the ASPECT developers to replace the simple.cc material model after it had gone through several modifications. However, simpler.cc still needed slight modification to use a Frank-Kamenetskii rheology [18, 19, 21]. Tests at 6 and 7 global refinements would not run to completion, so the linear solver tolerance was relaxed from 10^{-7} to 10^{-3}. As in cases 1a-1c, ASPECT asymptotically approaches Christensen's extrapolated values. Values of V_{RMS} and Nusselt number for all tests are in Table 3.5.

Tests of case 2a are less consistent. The cases with 3 global refinements and 4 global refine-

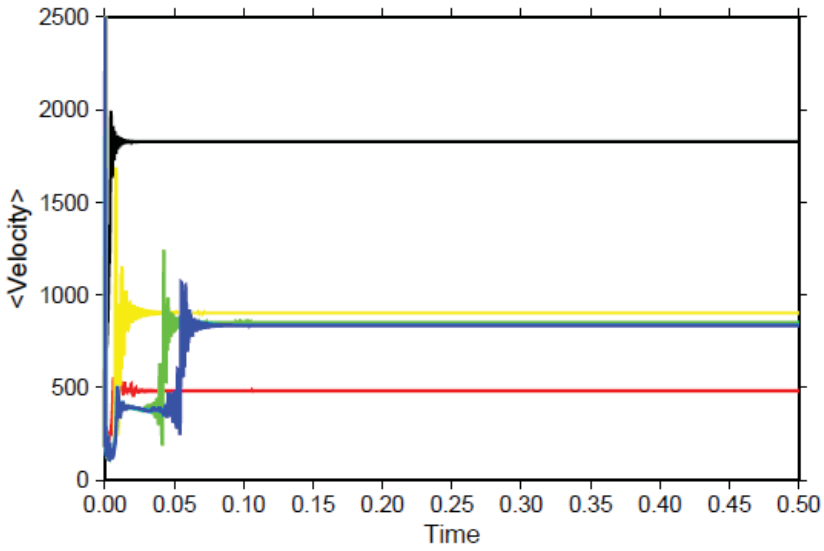

Figure 3.4: Root mean square (RMS) velocities from case 1c of Blankenbach et al. [2] at global refinements 3 (black), 4 (red), 5 (yellow), 6 (green), and 7 (blue).

ments both show oscillations smaller than 0.0001%. Unexpectedly, the case with 5 global refinements shows unstable, oscillating behavior of roughly 300 meters per second throughout the run (see Figure 3.6). Though unexpected, these perturbations in the case with 5 global refinements are consistent, and they average to values comparable to Christensen's extrapolated values (see Table 3.5). This behavior differs from other convection codes, which report no such oscillations. The values of V_{RMS} and Nusselt number from the calculations at 6 and 7 refinements are stable and values agree with Christensen's extrapolated values (Table 3.5).

Next, I test the Boussinesq Formulation using the same cookbook convection box case with the Boussinesq Approximation turned on. Nothing else is changed, as this case is already Boussinesq, so I expect using the new formulation will not change the outcome. This case is run with all non-dimensional terms, except α and g as described previously, at a global refinement of 4 to match the case in the ASPECT manual. The results match case 1a at 4 global refinements reported previously (Table 3.2), and the results presented in the manual.

Table 3.5: Blankenbach et al. [2] Benchmark 2a: Steady State, 2D, temperature-dependent viscosity convection (b=6.907755279) in a 1 by 1 box with Rayleigh number 10^4.

Code	Grid	Global Refinement	V_{RMS}	Nusselt No.
ConMan	50x50		488.950	10.080
ConMan	100x100		482.583	10.070
ConMan	200x200		480.879	10.067
ConMan	400x400		480.493	10.066
‡ASPECT	8x8	3	1280.542	6.362
‡ASPECT	16x16	4	683.608	9.529
‡ASPECT	32x32	5	561.690	8.928
‡ASPECT	64x64	6	499.622	10.078
‡ASPECT	128x128	7	482.695	10.080
†C_{ext}			480.433	10.066
‡CFL number 1.0, and solver tolerance 10^{-7} for global refinements 3 through 5, CFL number 1.0 and solver tolerance 10^{-3} for global refinements 6 and 7. †Christensen′s extrapolated values.				

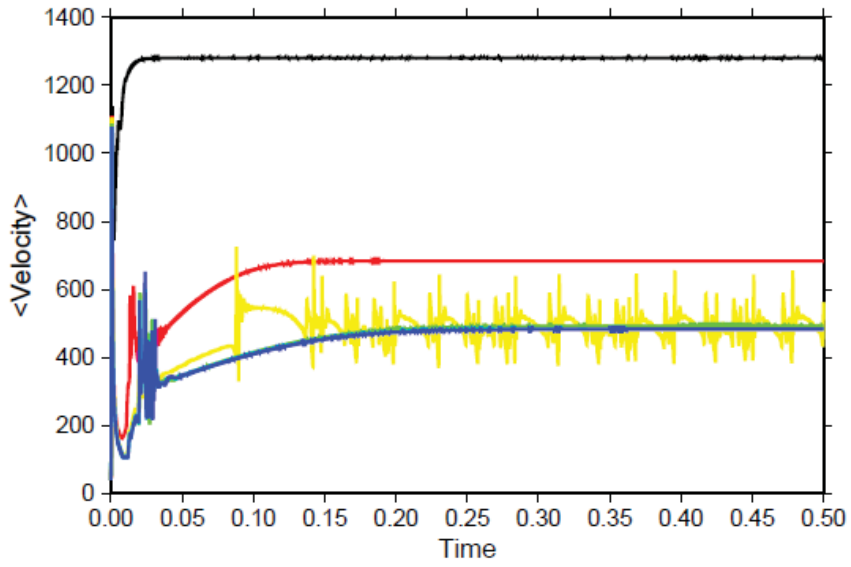

Figure 3.5: Root mean square (RMS) velocities from case 2a of Blankenbach et al. [2] at global refinements 3 (black), 4 (red), 5 (yellow), 6 (green), and 7 (blue).

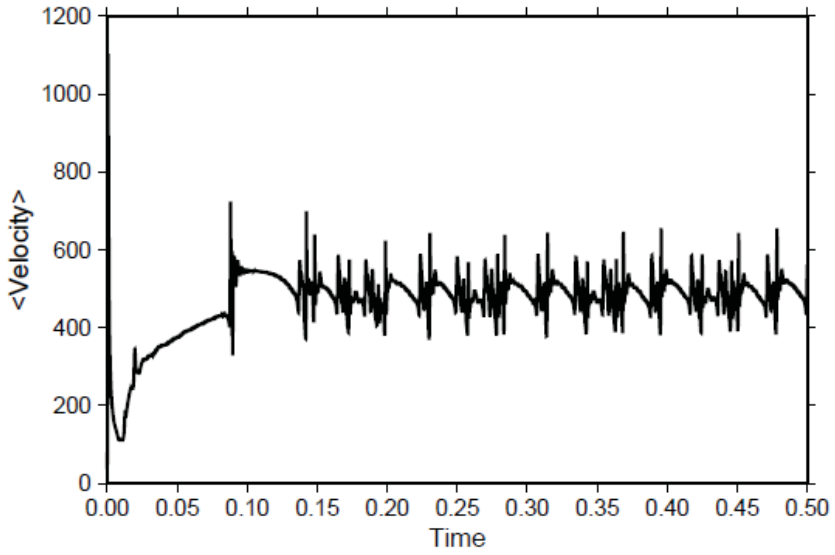

Figure 3.6: Root mean square (RMS) velocity from case 2a of Blankenbach et al. [2] at 5 global refinements. This behavior is different compared to other tests of this case; however, average values calculated are still comparable to Christensen's extrapolated values.

The velocity figure, Figure 3.7, is generated for comparison. I note that though the results match well on the scale of Figure 3.7, the small-scale oscillations are noticeably different. These oscillations are smaller, on the order of 0.0000001%, more well-behaved, and show an overall damping with time (Figure 3.8).

3.2 2D Boussinesq Case: Rayleigh-Taylor Instability in van Keken et al. [31]

Further testing using 2D is done to ensure that the Boussinesq formulation and my installation can reproduce published results for 2D. For this case I use the van Keken et al. [31] benchmark. The cases in this paper are similar to Blankenbach et al. [2]. Both deal with cases in a 2D Cartesian box containing a Boussinesq fluid at infinite Prandtl number. However, Blankenbach et al. [2] deals purely with thermal convection cases, whereas van Keken

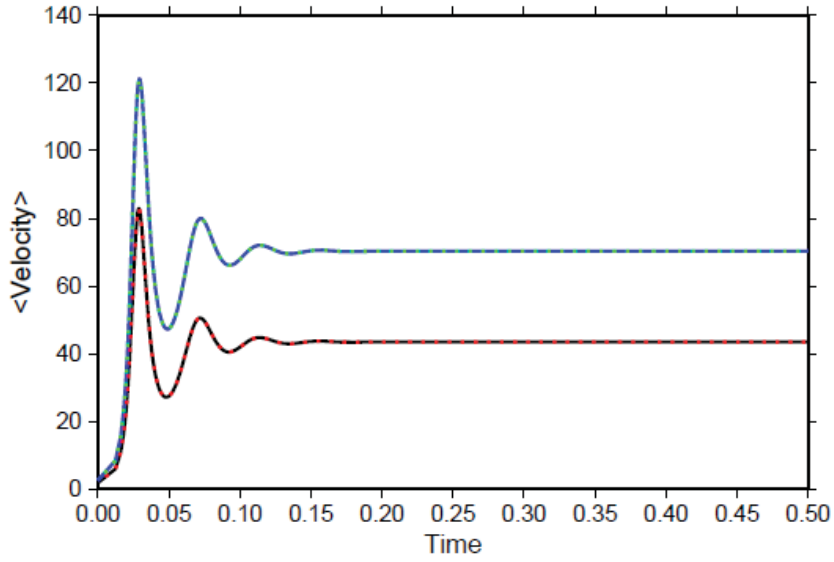

Figure 3.7: Root mean square (RMS) and maximal velocity from the original case 1a of Blankenbach et al. [2] using original conditions as well as the Boussinesq Approximation formulation in ASPECT. RMS and maximal velocities for the original case are shown in black and blue, respectively. RMS and maximal velocities for the case using the Boussinesq Approximation formulation are shown in dotted red and green, respectively.

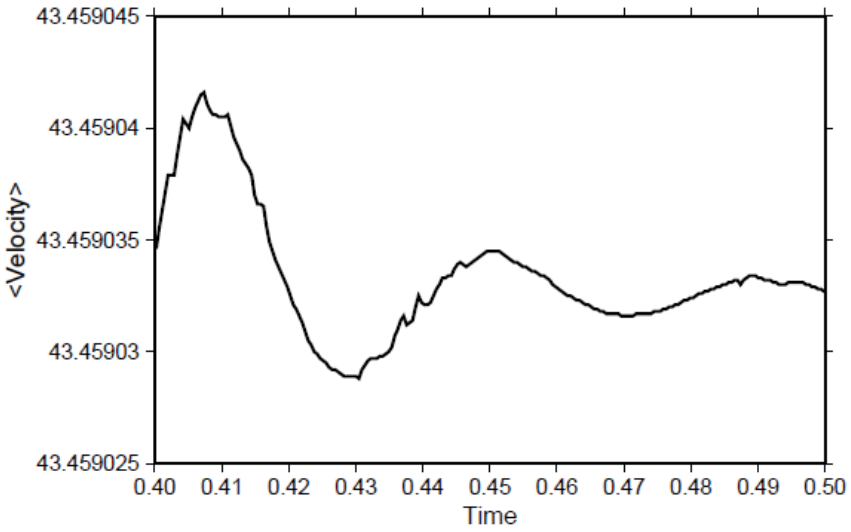

Figure 3.8: Small-scale oscillations for Blankenbach et al. [2] case 1a at global refinement 4 using the Boussinesq Approximation formulation in ASPECT. The plot is zoomed in to the final portion of the run, non-dimensional time 0.4 to 0.5. Oscillations are all smaller than 0.0000001% and are damping with time.

et al. [31] tests thermochemical convection, taking a difference in composition into account. This increases the difficulty of the problem, as chemical heterogeneities have to be tracked and compositional buoyancy forces have to be added to the equations of motion. However, the case tested in the ASPECT manual is case 1a from the paper, which is only for testing a chemical instability. The full name for case 1a is Isothermal Rayleigh-Taylor Instability. The set-up for case 1a is a 2D Cartesian box of dimensions $[0, \lambda] \times [0, 1]$, where λ is called the aspect ratio. The fluids in this problem are incompressible, i.e. $\nabla \cdot \nu = 0$. The paper calculates the thermal Rayleigh number, Ra, and the compositional Rayleigh number, Rb. Ra is given as the same as in [2], $Ra = \frac{\alpha g \Delta T D^3}{\kappa \nu_r}$. Rb is given as, $Rb = \frac{\Delta \rho g D^3}{\kappa \nu_r}$. This case has only two layers, meaning Γ is a step function equaling 1 in the initially lower layer and 0 in the other layer. Chemical diffusion is neglected for this problem, which correlates to an infinite Lewis number. The initial boundary between the two layers is described by $\omega = 0.02 \cos(\frac{\pi x}{\lambda})$. For this case, the aspect ratio, λ, was chosen to be 0.9142, because in a constant viscosity case a harmonic perturbation of wavelength 2λ is the most unstable and gives the largest growth rate. The top and bottom boundaries are rigid, which causes the fluids to stick to these boundaries. This causes secondary and tertiary diapirs to form. The side boundaries are reflective, allowing smooth movement towards the top or bottom. The viscosity of the buoyant, initially lower layer is given as η_0, and the viscosity of the dense layer as η_r. For case 1a, the ratio between the two is $\frac{\eta_0}{\eta_r} = 1$.

In the ASPECT manual, I note there is good agreement between tests at global refinements 5-9 and the cases from the benchmark paper; however, there is a larger discrepancy for the rising of the secondary and tertiary diapirs. This is due to the fact that the boundary as described by $\omega = 0.02 \cos(\frac{\pi x}{\lambda})$ is discontinuous, it moves in a stepping pattern. To fix this, the authors for the manual suggest using a different equation to smooth out the boundary between the layers. This smooth model is the test done in this work, and the boundary is

given by $\omega = \frac{1}{2}(1 + \tanh((0.2 + 0.02\cos(\frac{\pi x}{\lambda}) - z)/0.02))$. A case using 9 global refinements is run for its clear resolution. Besides the global refinement change, all other parameters are left as they come in the ASPECT code for this initial run. These results match those published in the ASPECT manual. A plot of the root mean square velocity is generated for comparison. The manual contains a plot of several root mean square velocity curves for different global refinements. The curve from this test and the 9 global refinements curve in the manual match well.

Again, as with the convection box tests, the same van Keken et al. [31] smooth case then had the Boussinesq Approximation turned on and it was rerun. This case also should be Boussinesq by design, so results are expected to be unchanged. It can be seen in Figure 3.9 that, once again, the results are the same as the published results. The value for the primary peak in V_{RMS}, which corresponds to the rising of the first diapir, for both the original case and the case using the Boussinesq formulation is 3.099×10^{-3}. This value matches to 11 decimal places, after which the value for each decimal place is reported as 0.

3.3 2D Boussinesq Case: Cylindrical Coordinates in Davies et al. (in preparation)

Continuing in 2D, my next test shifts away from Cartesian domains and begins to address spherical geometry. The previous 2D benchmarks both operate within boxes in the Cartesian plane. The Davies et al. paper, which is in preparation, but described in the ASPECT manual, uses a 2D, spherical Earth. This means that these cases run in a cylindrical domain. These cases already run using the Boussinesq Approximation. Case 2.1 is run at global refinements 2, 3, 4, and 5 and compared with results reported in the ASPECT manual. The

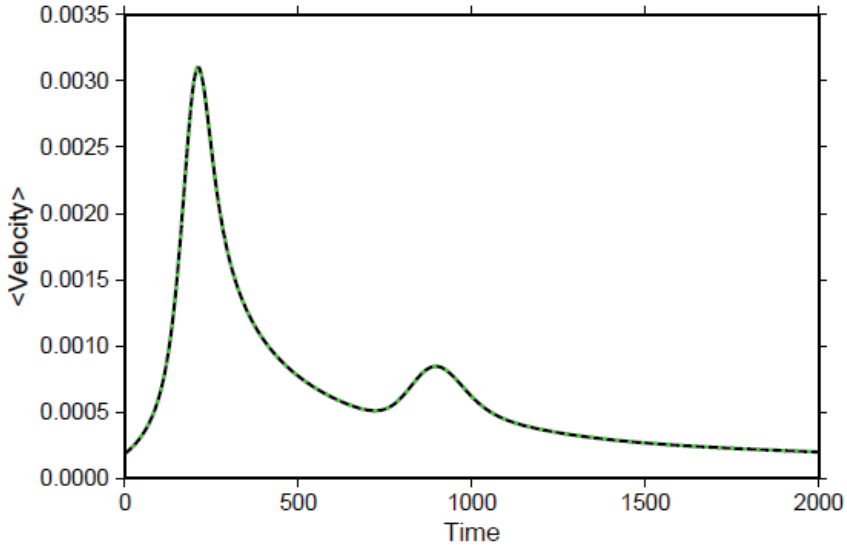

Figure 3.9: Root mean square (RMS) velocity from the smooth version of the van Keken et al. [31] benchmark at 9 global refinements. The original case is the black line, while the case using the Boussinesq Approximation formulation in ASPECT is shown by the green dots.

figures generated are the root mean square velocity curve of case 2.1 at 4 global refinements, and a visualization of the final time state of case 2.1. Both agree well with results described in the manual as seen in Table 3.6. In section 5.4.12 of the manual, this is described as a challenging problem for ASPECT, requiring many levels of refinement. The manual mentions that the input files for this problem in ASPECT start at 5 global refinements, but 7 global refinements are needed to achieve reasonable accuracy. At global refinement 4, the case shows agreement to the values presented in the ASPECT manual to within 3%. At global refinement 5, the case agrees to within 1%. This problem constitutes ongoing work of other ASPECT users. I include these results because it allows me to test a 2D, yet spherical case, representing an interesting middle ground between 2D boxes and 3D spherical shells.

As a test to see how ASPECT would function, case 2.1 is rerun at global refinements 2 through 5, but this time using a Rayleigh number of 7000 to match that used for the 3D spherical tests of the Zhong benchmark. The final comparison between the original case 2.1,

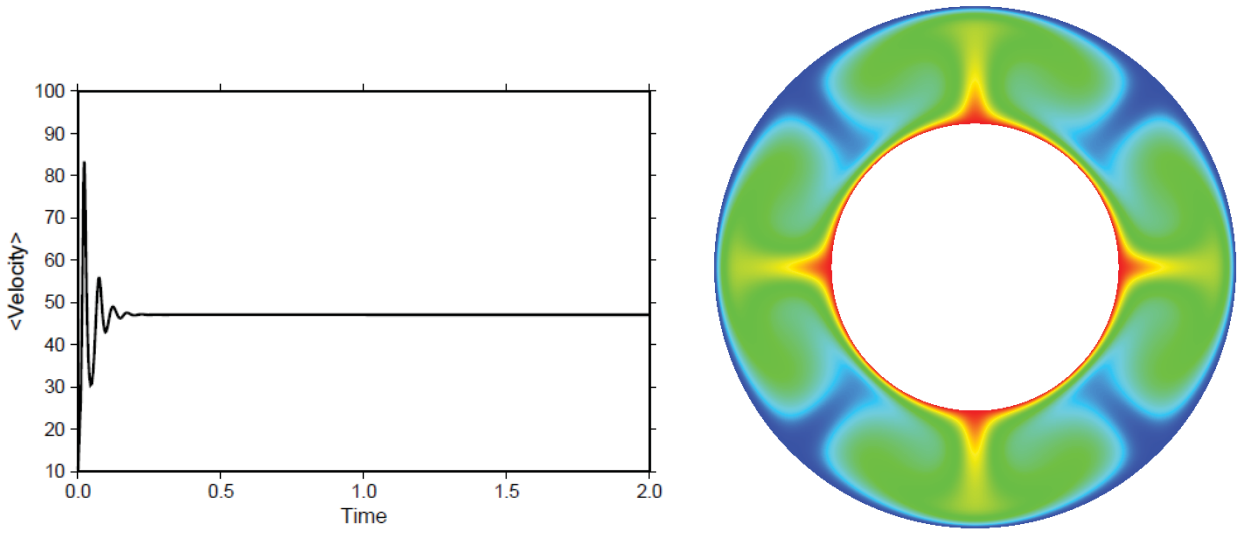

Figure 3.10: Root mean square (RMS) velocity for case 2.1 from Davies et al. (in preparation) (left). A slice from the temperature field at the final timestep for case 2.1 (right). Both of these are recreated using values calculated from ASPECT.

which had a Rayleigh number of 10000, and the new version is shown in Table 3.6. The original case 2.1 shows a large change going from 2 to 3 global refinements, then a leveling off at 4 and 5. The new versions remain more stable at all global refinements, showing a small decrease both in root mean square velocity and temperature going from 2 to 5 global refinements. The only exception is in the transition from 4 to 5 global refinements. In this case, the temperature increases by 0.01%.

3.4 3D Boussinesq Testing: "The A Family," Tetragonal Cases in Zhong et al. [35]

Zhong et al. [35] describes a number of different benchmark cases, including instantaneous Stokes flow, thermal convection, and thermochemical convection. In this section I focus on the cases labeled A1-A9. I call these the "A Family" and they are low Rayleigh number cases

Table 3.6: Results for Case 2.1 from Davies et al. (in preparation) on all refinements tested. Columns labeled 'Diff(%)' represent the percent difference between calculated values and values reported in the ASPECT manual. Every percent difference column refers to the value to its left.

Global Refinement	$\langle V_{RMS} \rangle$	Diff(%)	$\langle T \rangle$	Diff(%)
2	1390.9	2907.6	0.31609	-17.255
3	88.168	90.658	0.29631	-22.432
4	47.217	2.104	0.37748	-1.182
5	46.466	0.480	0.38431	0.603
‡2	37.101		0.38691	
‡3	35.688		0.38024	
‡4	35.083		0.37888	
‡5	35.040		0.37892	
†Davies	46.244		0.382	
†Case 2.1 values reported in the ASPECT manual. ‡Rayleigh number 7000 used.				

in tetragonal planform with increasing viscosity contrast. The first three cases, A1-A3, are also presented by Stemmer et al. [26], Ratcliff et al. [22], and Yoshida and Kageyama [32]. The A1-9 cases use a Rayleigh number of 7000 with a free-slip inner shell and outer shell velocity boundary conditions and constant temperature boundary conditions with $T = 0$ on the outer spherical boundary and $T = 1$ on the inner spherical boundary. The thickness of the mantle is set to 0.45, the inner boundary, r_i, is 0.55 and the outer boundary, r_o, is 1.0. All cases have a different temperature-dependent viscosity, $\Delta\eta$, given by

$$\eta = e^{E(0.5-T)}, \tag{3.4}$$

where E is a viscosity parameter similar to activation energy and T is temperature. Case A1 uses $\Delta\eta = 1$, A2 uses $\Delta\eta = 10$, A3 uses $\Delta\eta = 20$, A4 uses $\Delta\eta = 10^2$, up to A9 using $\Delta\eta = 10^7$. The equations use the Boussinesq approximation, hence density is constant everywhere except in the buoyancy term (see Chapter 2). The benchmark uses a spherical harmonic perturbation to initiate the pattern of convection generated in each case. These tests use a

spherical harmonic perturbation of degree 3 order 2 with a magnitude of perturbation for the cosine and sine terms of $\epsilon_c = \epsilon_s = 0.01$ to create a tetragonal pattern to match Zhong et al. [35] (Figure 3.11). The values for root mean square velocity, temperature, and Nusselt numbers at the top and bottom of the shell are averaged over the specific time intervals as reported in Zhong et al. [35]. I calculate these same values for each case over the respective intervals. For case A1, this interval is non-dimensional time 0.7 to 1. See Table 3.8 for the other time intervals as well as a listing of all cases and their associated results as documented in Zhong et al. [35].

I made modifications to ASPECT to allow testing conditions to be as similar as possible between CitcomS and ASPECT. The version of ASPECT used is 2.0.0-pre. Two main files are modified: the material model simple.cc and the initial temperature condition harmonic_perturbation.cc, as well as their accompanying header files simple.h and harmonic_perturbation.h, respectively. The initial temperature condition is modified such that two spherical harmonic perturbations can be used at the same time. This is necessary to reproduce the later cases, as two spherical harmonic perturbations are necessary to reproduce the correct end-state patterns. See section 3.5 for the full description of these cases. The file harmonic_perturbation.cc was copied and renamed to conductive_harmonic_perturbation.cc where these changes are enacted. The material model is changed to allow two different reference temperatures to be input. The temperature-dependent viscosity law this benchmark uses (Equation 3.4) requires a reference term of 0.5, however the temperature should be set to 1.0 for the remainder of the problem. The material model simple.cc was copied to simple_second.cc where these changes are enacted.

It should also be noted that the grid I use for most of the tests is not the default grid for ASPECT. ASPECT is designed to run using a grid that has cells that vary in spacing in the radial direction. That is, cells are radially smaller towards the center of the spherical

shell, and larger at the outer edge. It is also designed to use quadratic solver elements and adaptive mesh refinement by default. CitcomS by comparison, uses linear solver elements which are constant spacing throughout the mesh. CitcomS was used to calculate the results reported in Zhong et al. [35]; however, the authors refined the grid at the top and bottom, so their grid is not strictly uniform. In order to make the results calculated from ASPECT comparable to CitcomS such that the results could be benchmarked, cases are run using a grid that has cell spacing in the radial direction held constant, and adaptive mesh refinement turned off. The quadratic elements are still used. This grid is henceforth referred to as the radially-uniform grid, and is the grid used for all cases described unless otherwise stated. Cases A1, A3, and A7 are chosen to be run using a more ASPECT-like grid as well as the radially-uniform grid. This ASPECT-like grid is the same as the radially-uniform grid, except the cells are allowed to have variable spacing in the radial direction, as is the default for ASPECT. Adaptive mesh refinement is turned off. This means that this ASPECT-like grid is the default setting for ASPECT except for the adaptive mesh refinement. Despite this one difference, this ASPECT-like grid is henceforth known in this work as the ASPECT default grid.

3.4.1 3D Results for the Mobile Lid Cases: A1 through A5

Case A1 is run on the radially-uniform grid at 12×8^3, 12×16^3, 12×32^3, and 12×64^3 resolution. See Table 3.8 for parameters used for these tests. Cases are run using both $D = 1.0$ and $D = 0.45$. For cases where $D = 1.0$, $r_i = 1.22$ and $r_o = 2.22$. For cases where $D = 0.45$, $r_i = 0.55$ and $r_o = 1.0$. They are also run using velocity and temperature polynomial combinations: (1.0,1.0), (2.0,1.0), and (2.0,2.0). These determine whether linear (1.0) or quadratic (2.0) elements are used. CitcomS uses linear elements, while ASPECT can use either, though quadratic is the default. Cases are run using CFL number 1.0, except

Table 3.7: Parameters used in Zhong et al. [35] experiments. Unless otherwise stated, these are the parameters for all cases run.

Parameter	Symbol	Value
thickness of mantle	D	0.45
density	ρ	1.0 kg/m^3
temperature difference	ΔT	1.0 K
thermal diffusivity	κ	1.0 m^2 s^{-1}
thermal expansion coefficient	α	1.0 K^{-1}
gravitational acceleration	g	$\frac{7000}{0.45^3}$ m s^{-1} for the A Family and B1 $\frac{100000}{0.45^3}$ m s^{-1} for the C Family
reference viscosity	η_0	1.0 Pa s
reference temperature	T_0	0.5 K
velocity polynomial		2.0
temperature polynomial		2.0
Stokes tolerance		10^{-3}
expensive Stokes solver steps		1000
CFL number		1.0 for Cases A1, B1, and the C Family 2.0 for Cases A2 and A3 3.0 for Cases A5 through A9 4.0 for Case A4

Table 3.8: Values of the A Family and C Family cases as reported in Zhong et al. [35].

Test Performed	t_1	t_2	$\langle V_{RMS} \rangle$	$\langle T \rangle$	Nu_t	Nu_b
A1	0.7	1.0	32.66	0.2171	3.5126	3.4919
A2	1.0	1.3	27.36	0.2360	3.2674	3.2491
A3	0.6	0.9	25.85	0.2432	3.1724	3.1548
A4	1.5	2.0	23.11	0.2653	2.9354	2.9205
A5	1.0	1.5	22.90	0.3124	2.5468	2.5352
A6	2.6	3.6	29.21	0.3511	2.0414	2.0327
A7	1.2	1.7	50.21	0.5039	2.7382	2.7431
A8	0.8	1.0	87.27	0.5461	3.0317	3.0685
A9	0.48	0.54	157.6	0.5953	3.5634	3.6076
B1	1.2	1.7	31.09	0.2176	3.6254	3.6016
C1	0.255	0.315	154.8	0.1728	7.8495	7.7701
C2	0.48	0.55	122.1	0.1908	7.0968	7.0505
C3	0.52	0.57	109.1	0.2011	6.7572	6.7182
C4	0.825	0.925	98.90	0.2168	6.4803	6.4362

Table 3.9: Results of the "A Family" and "C Family" cases, as well as Case B1, in Zhong et al. [35] using the radially-uniform grid at 12×32^3. See Table 3.7 for standard parameters used. Note that A9 would not converge, but its row is left in for completeness. Cases A1 and C1 are also run using the radially-uniform grid at 12×64^3 refinement.

Case	Steps	Cores	t(hrs)	$\langle V_{RMS} \rangle$	Diff(%)	$\langle T \rangle$	Diff(%)	Nu_t	Diff(%)	Nu_b	Diff(%)
A1	7057	120(5)	15.81	32.614	-0.142	0.21169	-2.494	3.0736	-12.496	3.4209	-2.034
†A1	14146	144(6)	210.5	32.642	-0.056	0.21522	-0.866	3.4341	-2.236	3.4866	-0.153
A2	5877	72(3)	43.06	27.234	-0.461	0.23294	-1.295	3.0056	-8.011	3.1937	-1.705
A3	4267	72(3)	31.67	25.700	-0.579	0.24059	-1.073	2.9451	-7.165	3.1032	-1.635
A4	5855	72(3)	46.11	23.010	-0.431	0.26421	-0.411	2.8098	-4.277	2.8795	-1.405
A5	8496	72(3)	62.22	22.857	-0.186	0.31221	-0.062	2.5045	-1.661	2.5100	-0.996
A6	30898	120(5)	141.0	29.033	-0.605	0.34952	-0.449	2.0378	-0.176	2.0048	-1.374
A7	20384	120(5)	94.40	54.119	7.785	0.52161	3.515	2.8977	5.826	2.6492	-3.425
A8	22712	120(5)	110.9	99.977	14.561	0.57423	5.152	3.3233	9.618	2.8136	-8.309
‡A8	32524	144(6)	135.8	96.975	11.121	0.56729	3.879	3.2435	6.985	2.7050	-11.846
A9	N/A	168(7)	N/A	N/A	N/A	N/A	N/A	N/A	N/A	N/A	N/A
B1	11908	96(4)	33.72	31.129	0.127	0.21288	-2.171	3.2809	-9.503	3.5223	-2.203
C1	20303	96(4)	46.67	160.62	3.759	0.14690	-14.991	4.3879	-44.099	7.0676	-9.041
†C1	38866	192(8)	364.7	155.68	0.569	0.16394	-5.125	6.1792	-21.279	7.5108	-3.337
C2	17347	96(4)	92.77	124.58	2.032	0.16673	-12.616	4.3116	-39.246	6.4666	-8.282
C3	20560	120(5)	93.31	111.09	1.827	0.17903	-10.975	4.2983	-36.389	6.1778	-8.043
C4	32965	192(8)	116.39	100.35	1.466	0.19888	-8.267	4.4250	-31.716	5.9609	-7.385

†Case uses a grid refinement of 12×64^3
‡Case uses ASPECT default grid

for a few cases using 0.5. See the discussion of the results of case A2 for a full description of the CFL number. Cases are also run using Stokes tolerance 10^{-3} and temperature tolerance 10^{-12}, though a few cases are run with Stokes tolerance 10^{-7}. The reduction in tolerance is done to reduce runtime, especially for the later, more expensive cases. Earlier testing of case A1 shows no significant loss in accuracy when using this relaxed tolerance. Rather than achieving a Rayleigh number of 7000 by scaling everything to 1.0 and using a gravity value of 7000 (or everything to 1.0, D to 0.45, and gravity to $\frac{7000}{0.45^3}$), a few cases are run scaling reference viscosity, η_0, to $\frac{1}{7000}$ (or $\frac{0.45^3}{7000}$). This still mathematically equals a Rayleigh number of 7000, but avoids the possibility of the pressure being influenced by a large value of gravity. This is done to ensure the pressure is not changing, and therefore not affecting the flow.

Many of the cases of A1 are run to determine which conditions produce results most in agreement with the benchmark, as well as which produce the least computationally expensive runs. A subset of these results are shown in Table 3.10. This information is used to decide what conditions and parameters to use in future, more computationally expensive cases. I determine that velocity and temperature polynomials both set to 2.0 produce the best results. I also determine that using gravity scaling versus viscosity scaling produces no significant difference in results. That is, using either a high value of gravity or a low value of viscosity to achieve the desired Rayleigh number makes no difference on the results calculated. Using a geometry $D = 0.45$ ($r_i = 0.55, r_o = 1.0$) results in runs that are computationally cheaper by several hours, thus this geometry is adopted for most future cases. This also matches the geometry used in the benchmark. Case A1 is also run on both grids described in Section 3.4: the radially-uniform grid and the ASPECT default grid. The best cases use the radially-uniform grid, and produce V_{RMS} and average temperature differences of 0.38% and -8.38% respectively for 12×16^3 resolution, -0.14% and -2.49% respectively for 12×32^3 resolution, and -0.06% and -0.87% respectively for 12×64^3 resolution. Radial plots of the V_{RMS} and

average temperature between runs calculated by CitcomS and runs calculated by ASPECT show the behavior with respect to depth matches between the two codes (Figure 3.12).

The constant viscosity in this case allows for little resistance to flow. This results in the initial spherical harmonic perturbation being the defining feature of the flow, causing the steady-state planform of case A1 to be tetragonal (Figure 3.11). This ease of flow allows for efficient convection and heat flux out of the system through the upper boundary. The authors of Zhong et al. [35] determined that this was representative of a mobile lid tectonic regime, such as Earth has. This can be seen in the radial plots for A1 (Figure 3.12) as V_{RMS} holds a value over 30 m/s at the surface of the shell. While the value 30 m/s is not reasonable for real mantle flow speeds, the fact that flow speeds increase towards the surface implies there is movement at the top of the shell. I interpret this as motion associated with the movement of the tectonic plates. Future cases will be shown to enter a new tectonic regime as the viscosity contrast continues to increase.

In order to compare the solve behavior of CitcomS and ASPECT, runs of A1 at various refinements are compared. The best results calculated using ASPECT are on the radially-uniform grid. Cases are run at 12×8^3, 12×16^3, 12×32^3, and 12×64^3 refinement. For CitcomS, cases are run at 12×16^3, 12×32^3, 12×64^3, and 12×96^3 refinement. It should be noted that results reported for CitcomS in Zhong et al. [35] were calculated on a 12×32^3 grid with double refinement at the top and bottom of the shell. While the majority of cases presented in this work have their results compared against the results of the benchmark, these log-log solver comparisons are normalized against an extrapolated, theoretically-infinite value calculated from the CitcomS and ASPECT runs preformed here, respectively. The extrapolated values for both codes are shown in Table 3.11 for all cases

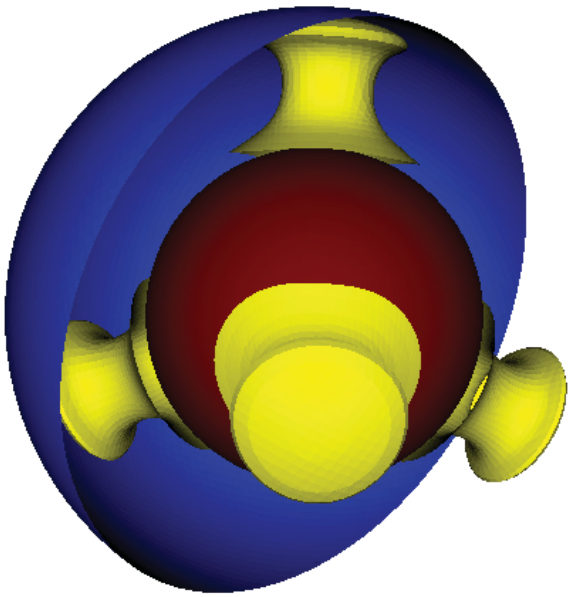

Figure 3.11: A series of isotherms generated from case A1 using a 12×32^3 radially-uniform grid. The dark red sphere represents the core, the yellow plumes are hotter, upwelling material, and the blue half-shell is the surface.

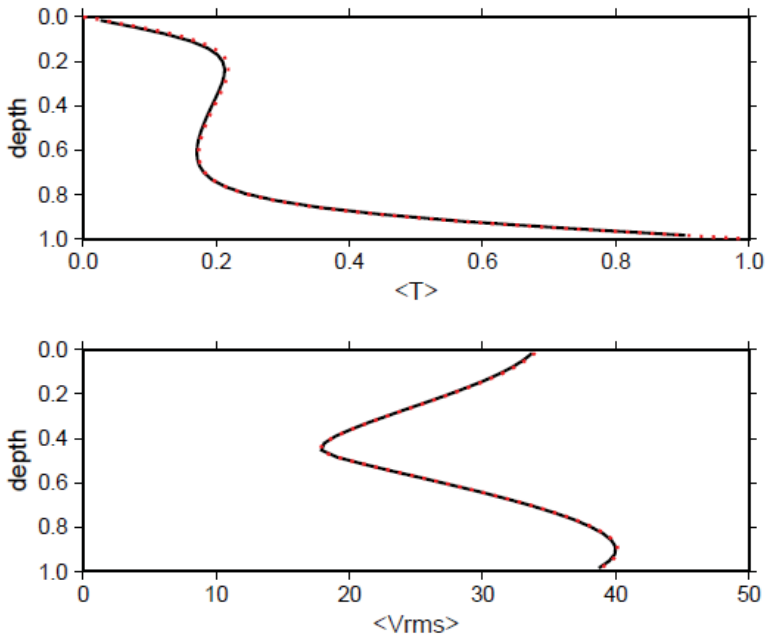

Figure 3.12: Average temperature and V_{RMS} with respect to depth of the shell of case A1. Results calculated from the radially-uniform grid in ASPECT are shown in black, and results calculated from CitcomS are shown in red dots.

Table 3.10: Results for Case A1 from Zhong et al. [35] on all grids tested. Columns labeled 'Diff(%)' represent the percent difference between calculated values and values reported in Zhong et al. [35]. Every percent difference column refers to the value to its left.

Case	Steps	Cores	t(hrs)	$\langle V_{RMS} \rangle$	Diff(%)	$\langle T \rangle$	Diff(%)	Nu_t	Diff(%)	Nu_b	Diff(%)
12×8^3	1261	24(1)	0.22	38.036	16.460	0.25390	16.949	2.4730	-29.596	3.1303	-10.354
12×16^3	3515	24(1)	4.06	32.787	0.389	0.19893	-8.368	2.4020	-31.616	3.2363	-7.321
12×32^3	7057	120(5)	15.81	32.614	-0.142	0.21169	-2.494	3.0736	-12.496	3.4209	-2.034
12×64^3	14146	144(6)	210.5	32.642	-0.056	0.21522	-0.866	3.4341	-2.236	3.4866	-0.153
‡12×8^3	1829	24(1)	0.31	39.088	19.681	0.25211	16.125	2.1560	-28.372	3.2088	-8.107
‡12×16^3	4134	24(1)	4.67	33.554	2.739	0.21797	0.399	2.5574	-27.193	3.2870	-5.869
‡12×32^3	9628	120(5)	21.81	32.538	-0.372	0.20954	-3.485	3.0225	-13.953	3.4359	-1.604
†Zhong				32.66		0.2171		3.5126		3.4919	

†Case A1 values reported in Zhong et al. [35].
‡ASPECT default mesh used.

Table 3.11: Extrapolated, theoretically-infinite values calculated for both CitcomS and ASPECT from runs at various grid refinements. These values are used to normalize the results calculated for their respective cases.

Code	Case	$\langle V_{RMS} \rangle$	$\langle T \rangle$
†CitcomS	A1	32.66	0.2171
†CitcomS	A3	25.85	0.2432
†CitcomS	A7	50.21	0.5039
CitcomS	A1	32.523	0.2125
CitcomS	A3	25.703	0.2408
CitcomS	A7	47.589	0.5120
ASPECT	A1	32.555	0.2216
ASPECT	A3	25.332	0.2457
ASPECT	A7	39.003	0.5076
†Original averaged values reported in Zhong et al. [35]			

compared. The normalized axis is presented on the plots as $|Vrms|$ or $|Temperature|$, where

$$|Vrms| = \frac{|V_{RMS,calculated} - V_{RMS,extrapolated}|}{V_{RMS,extrapolated}}. \tag{3.5}$$

The same formula is used to normalize the average temperature. Results for V_{RMS} and average temperature are then plotted in log-log space in order to see the slope produced by refining the different grids (Figure 3.13). As previously stated, ASPECT uses quadratic solver elements whereas CitcomS uses linear solver elements. In log-log space this should theoretically produce a slope of two for a quadratic function and one for a linear function. The slope for the CitcomS results at grid refinement 12×32^3 or finer do indeed produce slopes of roughly one. Likewise, ASPECT results at grid refinement 12×32^3 or coarser produce a steeper slope for V_{RMS}, though average temperature is not as steep.

Case A2 is run using both geometries, $D = 1.0$ and $D = 0.45$, on the radially-uniform grid at 12×32^3 resolution. These produce the exact same result: 1.11% difference from the value reported in Zhong et al. [35] for V_{RMS} and -0.60% for average temperature (Table 3.9). The planform is the standard tetragonal (see Figure 3.11).

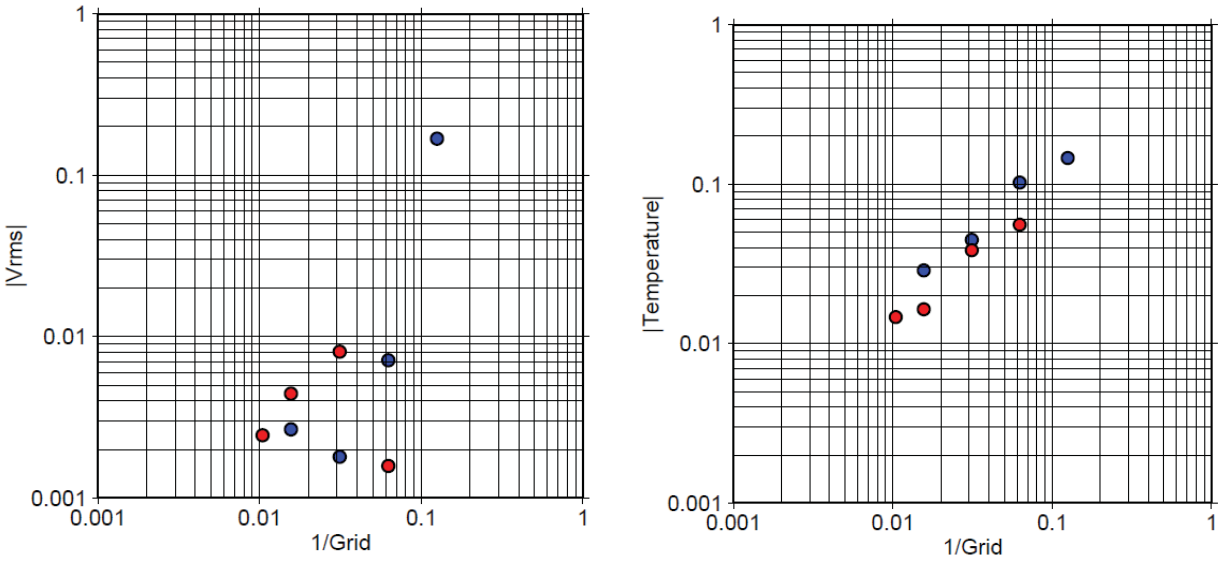

Figure 3.13: V_{RMS} and average temperature for cases of A1 run at various refinements using both CitcomS (red dots) and ASPECT (blue dots). Values are normalized (Equation 3.5) to extrapolated, theoretically-infinite values calculated from the CitcomS and ASPECT runs, respectively (Table 3.11). In both plots, the slope of the ASPECT results is steeper than CitcomS, as expected, though it is less pronounced in the average temperature.

In order to further reduce total computing time for later tests, cases of A2 are run using a CFL number of 1.0, the default for ASPECT, as well as 2.0, 3.0, 4.0, and 5.0. CFL stands for Courant-Friedrichs-Lewy number or condition. This condition is needed to ensure that finite element calculations are solved properly. The code must look at data from various grid cells to compute outputs; which takes a certain amount of in-case time. To ensure the outputs computed are accurate, the amount of in-case time needed to gather the data for computing the outputs at the points around the grid must be less than the in-case time required to move the problem forward to the next timestep. This ensures that the data from one grid point do not have time to influence the adjacent grid points before they are recorded. If the spacing between grid points is reduced, i.e. the grid is more resolved, the upper limit of the time-step will also reduce. The CFL number is chosen to define the maximum size of timestep allowable. Using a larger CFL number will allow the end time of the case to

be reached faster; however, the results may not be accurate. Case A2 is used to determine if larger CFL numbers could be used for later, more computationally expensive cases. See Table 3.12 for these results. Computing time goes down dramatically, from roughly 88 hours at CFL 1.0 to roughly 17 hours at CFL 5.0. These are compared and I found little change in values for V_{RMS} and average temperature. The case run at CFL 2.0 runs in roughly half the time, 43 hours, as the case using CFL 1.0, and has the closest values to case A2 in Zhong et al. [35], with -0.46% difference for V_{RMS} and -1.29% difference for average temperature. It is not fully understood why a CFL number of 2.0 gets the best agreement to the benchmark. It may be that the more relaxed solver conditions allow for a favorable averaging at this level. Note that the other CFL cases are all in good agreement and similar in values to the best case (Table 3.12).

Case A3 and all subsequent cases are run only using the $D = 0.45$ geometry. All tests agree with Zhong et al. [35]. Tests are run on 12×8^3, 12×16^3, and 12×32^3 radially-uniform grids (Table 3.14). As the grids become more refined, the RMS velocity and average temperature come into better agreement. The 12×8^3 grid has 2.28% difference for V_{RMS} and -7.96% difference for average temperature. The 12×32^3 grid has -0.58% difference for V_{RMS} and -1.07% difference for average temperature. The 12×16^3 grid obtains a V_{RMS} difference of -0.56%, slightly better than the 12×32^3 grid. Radial plots of A3 runs using CitcomS and ASPECT show good agreement (Figure 3.14), and the planform is tetragonal (Figure 3.15). Looking at the V_{RMS} radial plot, it can be seen that there is a value around 20 m/s at the top of the shell. This shows that this case is still in the mobile lid regime. The same CFL tests as described previously are run at the 12×32^3 grid for A3. Again, the higher CFL numbers greatly reduce the runtime while not significantly influencing the results. The test using CFL 2.0 produces the best results listed above for the 12×32^3 grid. Once again, this is not fully understood, but all CFL cases are in good agreement with each other(Table 3.13).

Table 3.12: Results of case A2 in Zhong et al. [35] using the radially-uniform grid at 12×32^3. Cases are run using CFL number 1.0 to 5.0. Note that the case using CFL 2.0 are the results reported in Table 3.9.

CFL	Steps	Cores	t(hrs)	$\langle V_{RMS} \rangle$	Diff(%)	$\langle T \rangle$	Diff(%)	Nu_t	Diff(%)	Nu_b	Diff(%)
1.0	11835	72(3)	88.34	27.185	-0.641	0.23206	-1.672	2.9491	-9.741	3.1924	-1.744
2.0	5877	72(3)	43.06	27.234	-0.461	0.23294	-1.295	3.0056	-8.011	3.1937	-1.705
3.0	3886	72(3)	27.33	27.1975	-0.5940	0.232209	-1.6064	2.9398	-10.027	3.1926	-1.739
4.0	2889	72(3)	20.56	27.1968	-0.5964	0.232201	-1.6097	2.9387	-10.060	3.1926	-1.739
5.0	2291	72(3)	16.58	27.1970	-0.5957	0.232208	-1.6068	2.9395	-10.034	3.1926	-1.739

Table 3.13: Results of case A3 in Zhong et al. [35] using the radially-uniform grid at 12×32^3. Cases are run using CFL number 1.0 to 4.0. Note that the case using CFL 2.0 are the results reported in Table 3.9.

CFL	Steps	Cores	t(hrs)	$\langle V_{RMS} \rangle$	Diff(%)	$\langle T \rangle$	Diff(%)	Nu_t	Diff(%)	Nu_b	Diff(%)
1.0	8624	72(3)	61.67	25.653	-0.764	0.23982	-1.389	2.8962	-8.706	3.1019	-1.676
2.0	4267	72(3)	31.67	25.700	-0.579	0.24059	-1.073	2.9451	-7.165	3.1032	-1.635
3.0	2810	72(3)	21.33	25.677	-0.671	0.24011	-1.271	2.9013	-8.544	3.1023	-1.663
4.0	2079	72(3)	14.78	25.671	-0.691	0.240106	-1.272	2.8946	-8.758	3.1022	-1.666

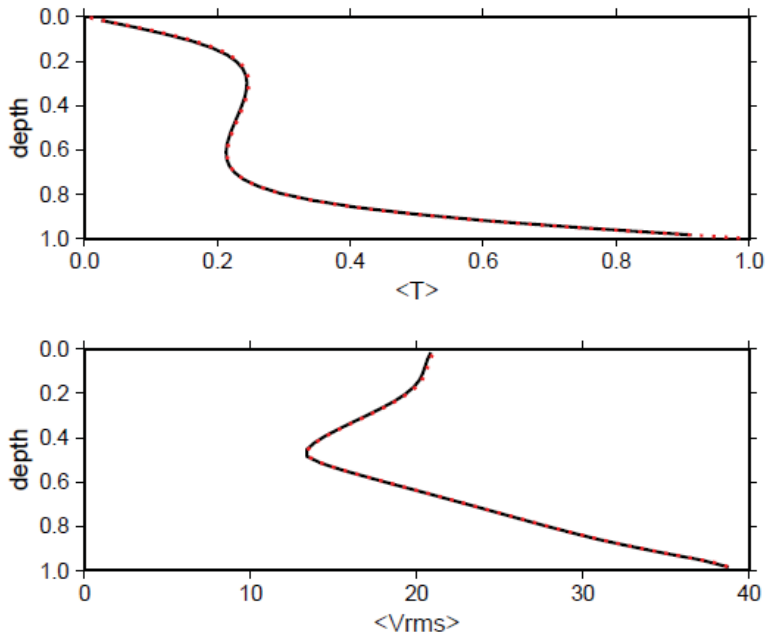

Figure 3.14: Average temperature and V_{RMS} with respect to depth of the shell of case A3. Results calculated from the radially-uniform grid in ASPECT are shown in black, and results calculated from CitcomS are shown in red dots.

Tests are also run to determine the differences in results achieved by the ASPECT default grid and the radially-uniform grid. The tests for A3 above use the radially-uniform grid, which has the same level of definition throughout its mesh. The ASPECT default grid is more refined at the base and less refined at the top. I hypothesize that this would make the radially-uniform grid better for the lower "A Family" cases, and the ASPECT default grid better for the higher, stagnant lid conditions, "A Family" cases. ASPECT default grids at 12×8^3, 12×16^3, and 12×32^3 resolutions are tested for A3. The results are in fair agreement, though they are slightly worse than the radially-uniform grid (Table 3.14). Values for V_{RMS} and average temperature using the ASPECT default grid at 12×32^3 resolution have a difference of -1.02% and -1.72%, respectively. At the same resolution, the radially-uniform grid has -0.58% and -1.07%, respectively. The ASPECT default grid is also used for some cases of A7 and A8 to test the stagnant lid hypothesis.

Table 3.14: Results for Case A3 from Zhong et al. [35] on all grids tested. Columns labeled 'Diff(%)' represent the percent difference between calculated values and values reported in Zhong et al. [35]. Every percent difference column refers to the value to its left.

Case	Steps	Cores	t(hrs)	$\langle V_{RMS} \rangle$	Diff(%)	$\langle T \rangle$	Diff(%)	Nu_t	Diff(%)	Nu_b	Diff(%)
12×8^3	843	72(3)	0.19	26.441	2.284	0.22384	-7.961	1.9402	-38.841	2.7999	-11.249
12×16^3	2047	72(3)	2.12	25.705	-0.562	0.23405	-3.762	2.4407	-23.064	2.9453	-6.641
12×32^3	4267	72(3)	31.67	25.700	-0.579	0.24059	-1.073	2.9451	-7.165	3.1032	-1.635
‡12×8^3	1210	72(3)	0.26	25.907	0.222	0.21728	-10.660	1.9055	-39.935	2.7253	-13.614
‡12×16^3	2892	72(3)	3.00	25.305	-2.107	0.22857	-6.017	2.3747	-25.144	2.9538	-6.372
‡12×32^3	5995	72(3)	42.22	25.587	-1.019	0.23901	-1.723	2.8992	-8.613	3.1119	-1.359
†Zhong				25.85		0.2432		3.1724		3.1548	

†Case A3 values reported in Zhong et al. [35].
‡ASPECT mesh used.

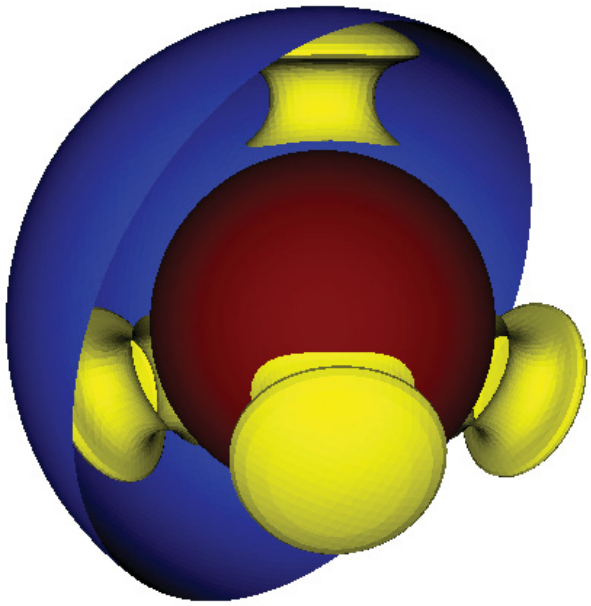

Figure 3.15: A series of isotherms generated from case A3 using a 12×32^3 radially-uniform grid. The dark red sphere represents the core, the yellow plumes are hotter, upwelling material, and the blue half-shell is the surface.

The same test of solver scope as was done for case A1 is also performed using various refinements of case A3. ASPECT results are run on radially-uniform grids of 12×8^3, 12×16^3, and 12×32^3 refinement. CitcomS results are run on grids of 12×16^3, 12×32^3, 12×64^3, and 12×96^3. Again, values are normalized to extrapolated, theoretically-infinite values using the results of the CitcomS and ASPECT runs (Table 3.11), and are plotted in log-log space (Figure 3.16). The results of the ASPECT cases produce slopes comparable to CitcomS results in this case. It should be noted that in the case of ASPECT, the V_{RMS} value of the case with refinement 12×32^3 do not agree with the extrapolated value as well as the value of the case with refinement 12×16^3. However, the temperature of these cases follows a more normal pattern. It should also be noted that the CitcomS values for V_{RMS} do not follow a linear trend, as can be seen even in this normalized plot (Figure 3.16).

Case A4 is run using the radially-uniform grid at 12×32^3 resolution. Cases are run using

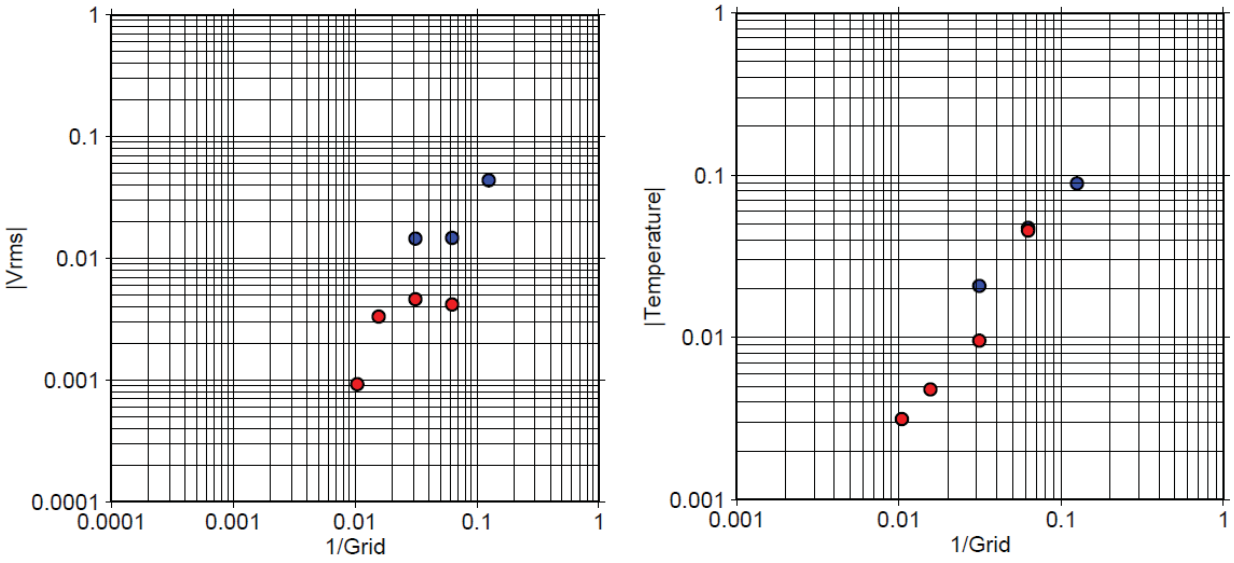

Figure 3.16: V_{RMS} and average temperature for cases of A3 run at various refinements using both CitcomS (red dots) and ASPECT (blue dots). Values are normalized (Equation 3.5) to extrapolated, theoretically-infinite values calculated from the CitcomS and ASPECT runs, respectively (Table 3.11). In both plots, the average slopes are relatively similar.

the $D = 0.45$ geometry. Once again, the CFL number is tested. Values 1.0 through 4.0 are used. It is again found that runtime is significantly reduced, 113 hours at CFL 1.0 versus 46 hours at CFL 4.0, while the results are not significantly changed. See Table 3.15 for results. The highest CFL case, 4.0, is in the best agreement to Zhong et al. [35]. The V_{RMS} has -0.43% difference while the average temperature has -0.41% difference. The planform is the standard tetragonal (see Figure 3.15).

The results of A2 through A4 show that the results are still accurate at CFL values higher than 1.0 while the runtime is significantly decreased. I determine at this point that the small change in results is worth the large decrease in overall runtime. The remaining cases of the A family are run using a CFL number of 3.0. This value is small enough that results are still well-defined, but runtime is greatly reduced.

Case A5 is run using the radially-uniform grid at 12×32^3 resolution. The case is run using

Table 3.15: Results of case A4 in Zhong et al. [35] using the radially-uniform grid at 12×32^3. Cases are run using CFL number 1.0 to 4.0. Note that the case using CFL 4.0 are the results reported in Table 3.9.

CFL	Steps	Cores	t(hrs)	$\langle V_{RMS} \rangle$	Diff(%)	$\langle T \rangle$	Diff(%)	Nu_t	Diff(%)	Nu_b	Diff(%)
1.0	23781	72(3)	113.1	22.944	-0.717	0.26339	-0.721	2.7577	-6.053	2.8775	-1.473
2.0	11837	72(3)	89.00	22.981	-0.558	0.26392	-0.519	2.7890	-4.986	2.8786	-1.434
3.0	7847	72(3)	60.12	23.003	-0.465	0.26415	-0.435	2.8061	-4.406	2.8793	-1.411
4.0	5855	72(3)	46.11	23.010	-0.431	0.26421	-0.411	2.8098	-4.277	2.8795	-1.405

the $D = 0.45$ geometry. The case is run on 72 cores and takes about 62 hours to run. The case has good agreement to the benchmark. The V_{RMS} has a difference of -0.19% and the average temperature has a difference of -0.06%. (see Table 3.9). This case has one of the best agreements to Zhong et al. [35] of all that are run. It should be noted that this is the last case that is tetragonal in planform. This case and all cases preceding it, A1-A4, reach the previously described tetragonal planform in their steady states (see Figures 3.11 and 3.15). Case A5 uses a viscosity contrast, $\Delta\eta$, of 1000. The next case marks a viscosity contrast high enough that the convective flow pattern changes, and the steady-state planform is altered as a result. All the remaining A Family cases, A6-A8, use the same degree 3 order 2 spherical harmonic perturbation as their initial condition, and therefore are called tetragonal cases. However, their steady-state planforms are not tetragonal in shape. They are distinct and represent more complex flow, as well as changing tectonic regime.

3.4.2 3D Results for the Transitional Case: A6

Case A6 is run using the radially-uniform grid at 12×32^3 resolution. The case is run using the $D = 0.45$ geometry using CFL number 3.0. The case is run on 120 cores and takes about 141 hours. This long runtime is partly due to the end time of the case being approximately three times as large as the other A family cases, going out to non-dimensional time 3.6. This is because this case is noted in Zhong et al. [35] as a transitional state where the planform begins to take on a stagnant lid convection regime. The earlier A Family cases have low viscosity contrasts. This allows easier flow, and therefore are in the mobile lid convection regime. The viscosity contrast for this case, $\Delta\eta = 10^4$, is high enough that the end-state time-evolution flow pattern is different than the standard tetragonal of the previous cases. This transitional case has all of its upwelling plumes migrate to one side of the sphere throughout the run. The final steady-state is a 50% split between mantle upwelling and

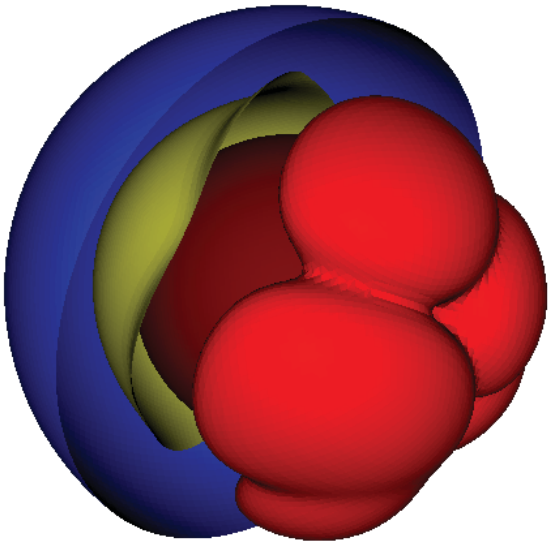

Figure 3.17: A series of isotherms generated from case A6 using a 12×32^3 radially-uniform grid. The dark red sphere represents the core, the bright red plumes are hotter, upwelling material, the yellow layer is colder, downwelling material, and the blue half-shell is the surface. Note that in this case all of the upwelling is on one side and all of the downwelling on the other.

downwelling (Figure 3.17). The results calculated for this case have good agreement to the benchmark. The V_{RMS} has a difference of -0.61% and the average temperature has a difference of -0.45%. This is the only case using the radially-uniform grid that has better agreement for the Nusselt number at the top of the shell than the Nusselt number at the bottom (Table 3.9).

3.4.3 3D Results for the Stagnant Lid Cases: A7 and A8

Case A7 is used as the other major test for the two ASPECT grid types as well as resolutions. It was chosen because it comes after the transitional case A6 and therefore within what Zhong et al. [35] defined as examples of stagnant lid behavior. It has the smallest $\Delta\eta$ of the three stagnant lid cases, A7-A9, so it was also chosen for its speed. Case A7 is run on both

the radially-uniform and ASPECT default grids at resolutions of 12×8^3, 12×16^3, and 12×32^3. Cases are run using a CFL number of 3.0 and the $D = 0.45$ geometry. As stated in Section 3.4.1, the hypothesis here is that the ASPECT default grid should get an answer more in agreement in these stagnant lid cases due to its increased resolution at the base of the spherical shell.

Cases for both ASPECT default and radially-uniform grids at the highest resolutions run, 12×32^3, have good agreement, but as expected the ASPECT default grid has better agreement overall (Table 3.16). For the radially-uniform grid the V_{RMS} agreement is 7.78% and the average temperature agreement is 3.51%. The ASPECT default grid at the same resolution got agreements at about three times closer. V_{RMS} agreement is 2.43% and the average temperature is 1.86%. Likewise, the lower resolution cases have better agreement using the ASPECT default grid versus the radially-uniform grid. The agreements in these cases are fair to poor, but the pattern still stands. Radial plots between runs using CitcomS and the ASPECT default grids show different patterns for average temperature and V_{RMS} than previous cases (Figure 3.18), though both codes are still in good agreement. The V_{RMS} radial plot now shows the value going to 0 as the top of the shell is reached. This implies there would be little movement of the surface, which is indicative of the stagnant lid tectonic regime. As stated in Section 3.4.2, the steady-state planform is now different. Convection is now more vigorous, with more hot material upwelling throughout the mantle in several, smaller plumes (see Figure 3.19), as opposed to the few, large-scale plumes of cases A1 through A5. This behavior matches the behavior reported in Zhong et al. [35].

Due to the increased viscosity contrast, $\Delta\eta$, I hypothesized that some form of averaging could stabilize the lower refinement cases of A7 and cause even better agreement for the 12×32^3 resolution. To test this, the cases using the ASPECT default grid at 12×8^3 and 12×16^3 resolution are re-run using harmonic averaging. This does influence the answers

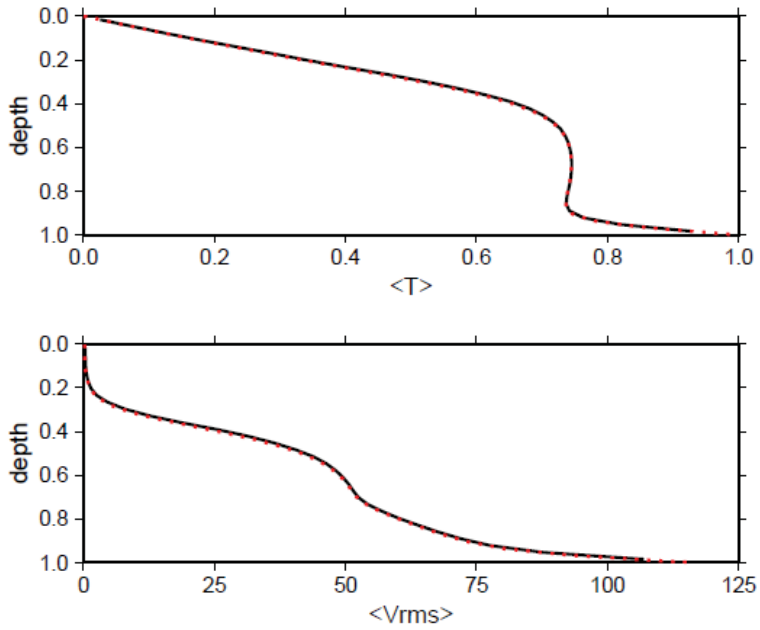

Figure 3.18: Average temperature and V_{RMS} with respect to depth of the shell of case A7. Results calculated from ASPECT default grid are shown in black, and results calculated from CitcomS are shown in red dots.

to a significant degree; however, the agreement to Zhong et al. [35] does not improve (see Table 3.16). Based on these results, I determined that testing harmonic averaging with the 12×32^3 ASPECT default grid is not worth the computing time.

Case A7 is also used as the stagnant lid case to test the solver behavior for CitcomS and ASPECT. This is done in the same manner as for cases A1 and A3: cases run at various refinements using CitcomS and ASPECT have their results for V_{RMS} and average temperature normalized against extrapolated values calculated from the CitcomS and ASPECT runs (Table 3.11). These results are then plotted in log-log space (Figure 3.20). For ASPECT, these runs are at 12×8^3, 12×16^3, and 12×32^3 refinement. For CitcomS, the runs are at 12×16^3, 12×32^3, and 12×64^3 refinement. Slopes for both of these data sets are more similar than the mobile lid cases; however, the results calculated by ASPECT still have a steeper slope than the results calculated by CitcomS. The ASPECT results for average temperature

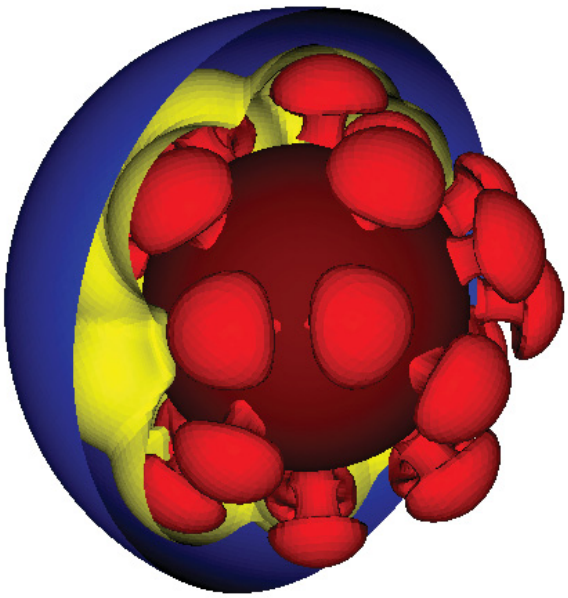

Figure 3.19: A series of isotherms generated from case A7 using a 12×32^3 ASPECT mesh. The dark red sphere represents the core, the bright red plumes are hotter, upwelling material, the yellow layer is colder material, the pockets of which show downwelling, and the blue half-shell is the surface.

Table 3.16: Results for Case A7 from Zhong et al. [35] on all grids tested. Columns labeled 'Diff(%)' represent the percent difference between calculated values and values reported in Zhong et al. [35]. Every percent difference column refers to the value to its left. Two cases are rerun using Harmonic Averaging to see if that could further refine results.

Case	Steps	Cores	t(hrs)	$\langle V_{RMS} \rangle$	Diff(%)	$\langle T \rangle$	Diff(%)	Nu_t	Diff(%)	Nu_b	Diff(%)
12×8^3	9835	120(5)	2.71	153.14	204.99	0.59456	17.991	5.4410	98.709	1.2195	-55.543
12×16^3	12198	120(5)	8.99	64.685	28.829	0.51843	2.884	3.0397	11.010	2.2822	-16.801
12×32^3	20384	120(5)	94.40	54.119	7.785	0.52161	3.515	2.8977	5.826	2.6492	-3.425
‡12×8^3	12372	120(5)	3.08	119.65	138.30	0.52110	3.414	4.2438	54.985	1.3810	-49.657
‡‡12×8^3	11705	120(5)	3.11	54.254	8.055	0.30672	-39.131	1.4214	-48.090	1.4965	-45.444
‡12×16^3	18070	120(5)	13.93	63.859	27.184	0.50975	1.160	3.0521	11.462	2.2057	-19.590
‡‡12×16^3	17228	120(5)	13.53	66.103	31.653	0.48453	-3.844	3.0495	11.370	2.2347	-18.533
‡12×32^3	28237	120(5)	131.0	51.431	2.432	0.51326	1.858	2.8338	3.492	2.6374	-3.852
†Zhong				50.21		0.5039		2.7382		2.7431	

†Case A7 values reported in Zhong et al. [35].
‡ASPECT mesh used.
‡‡ASPECT mesh with Harmonic Averaging used.

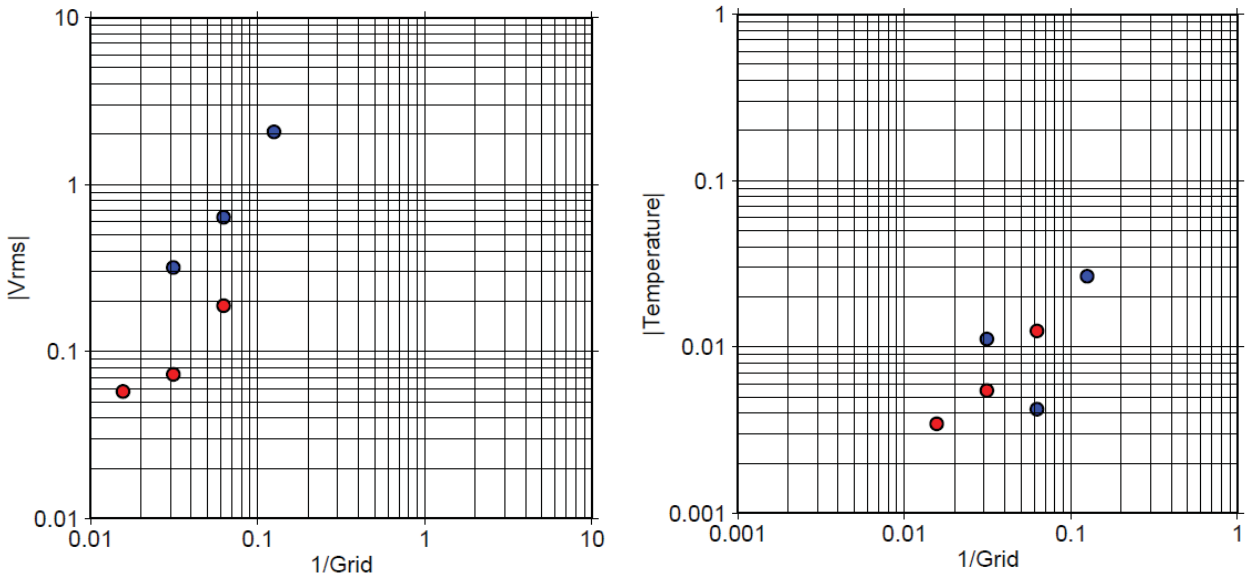

Figure 3.20: V_{RMS} and average temperature for cases of A7 run at various refinements using both CitcomS (red dots) and ASPECT (blue dots). Values are normalized (Equation 3.5) to extrapolated, theoretically-infinite values calculated from the CitcomS and ASPECT runs, respectively (Table 3.11). In both plots, the slope of the ASPECT results is steeper than CitcomS, as expected.

do not have a linear trend, as can be seen.

Case A8 is run using both the radially-uniform grid and the ASPECT default grid at 12×32^3 resolution. They are run using CFL number 3.0 and the $D = 0.45$ geometry. The same hypothesis stands for case A8 as case A7: the ASPECT default grid should provide superior resolution for a stagnant lid regime with its radially varying cells. Agreements for both cases are fair, with V_{RMS} differences being about two times farther than average temperature. Agreement for the radially-uniform grid is 14.56% difference for V_{RMS} and 5.15% difference for average temperature. However, the ASPECT default grid gets better agreement with 11.12% difference for V_{RMS} and 3.88% difference for average temperature (Table 3.9). The steady-state pattern is more complex with many smaller mantle upwellings across the shell (see Figure 3.19). Case A8 appears to represent more complex flow than A7, which may help explain the poorer agreement of the results calculated for A8 and the results reported

in Zhong et al. [35].

Case A9 fails to run using the same conditions as the previous A family cases. The case is designed with the radially-uniform grid at 12×32^3 resolution using a CFL number of 3.0 and the $D = 0.45$ geometry. The case does not have any errors associated with it. The case runs for several timesteps, then hangs for the remainder of the runtime attempting to solve the Stokes' system. A few other A family cases had this issue, which could be solved by allowing more expensive solver steps. One case of A9 using expensive steps increased from 1000, the default, to 147483647 was tried. This value is chosen by looking at the maximum value allowable, and reducing it by roughly an order of magnitude. This runs for several days with no progress made. Case A9, tetragonal with $\Delta\eta = 10^7$, is abandoned after this attempt.

3.5 3D Boussinesq Testing: "The C Family," Cubic Cases in Zhong et al. [35]

The modifications performed to the initial temperature condition file harmonic_perturbation.cc, resulting in the new file conductive_harmonic_perturbation.cc, allow for two harmonic perturbations to be input simultaneously as initial conditions. This is done so that the C Family of cases can be run. The A Family uses a harmonic perturbation of degree 3, order 2 for their initial condition, which results in their steady-state tetragonal planforms. The C Family uses spherical harmonic perturbations degree 4, order 0, as well as degree 4, order 4 as their initial condition. This causes the number of major plumes to increase from 4 to 6. This results in the planform taking on a cubic shape. In the A Family tetragonal cases, the four major plumes can be seen as representing the four corners of a tetrahedron. In these new

cases, the six plumes are evenly spaced apart, and can be seen to be representing the centers of the six sides of a cube. Hence, they are referred to as cubic. The other major difference in these cases is that the Rayleigh number is increased to 10^5 versus 7000 for the A Family.

In order to test whether the new code modifications for using two spherical harmonic perturbations at once are working properly, one case of B1 is run. Case B1 uses the double harmonic perturbation of the C Family, but uses $Ra = 7000$ like the A Family. It is used here as a middle ground case to ensure the results for the C Family, as going from the A Family to case B1 to the C Family allows for only one major change in parameters at a time. It is run using a CFL number of 1.0 and the $D = 0.45$ geometry. Agreement for this case is similar to case A1: good for both V_{RMS} and average temperature, though V_{RMS} is better than average temperature. The agreement is 0.13% difference for V_{RMS} and -2.17% difference for average temperature (Table 3.9). The planform is cubic with six well-formed plumes (Figure 3.21). The C Family can now be run knowing the code is functioning correctly.

Case C1 is run on the radially-uniform grid at 12×32^3 resolution using a CFL number of 1.0 and the $D = 0.45$ geometry. The viscosity contrast throughout the shell is the same as case A1, $\Delta\eta = 1$. The results are expected to be similar to the low A Family cases, as the viscosity contrast is constant. However, results are farther from the benchmark than expected: fair for V_{RMS} and poor for average temperature. Agreement is 3.76% difference for V_{RMS} and -14.99% difference for average temperature (Table 3.9). The planform is cubic with slightly thinner plumes than those of case B1 (Figure 3.23). Radial plots of average temperature and V_{RMS} from CitcomS and ASPECT show a higher degree of separation than those of the A Family (Figure 3.22). The general behavior of both data sets with respect to depth is consistent however, with the shape of the curves matching for each.

It has been previously determined with the low A Family cases that the tolerance can be relaxed from its default value of 10^{-7} to 10^{-3} with no significant loss of accuracy but a

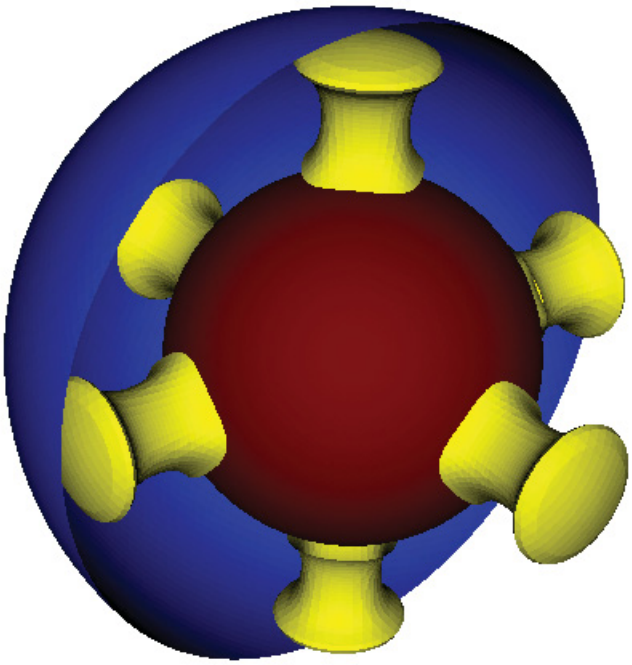

Figure 3.21: A series of isotherms generated from case B1 using a 12×32^3 radially-uniform grid. The dark red sphere represents the core, the yellow plumes are hotter, upwelling material, and the blue half-shell is the surface.

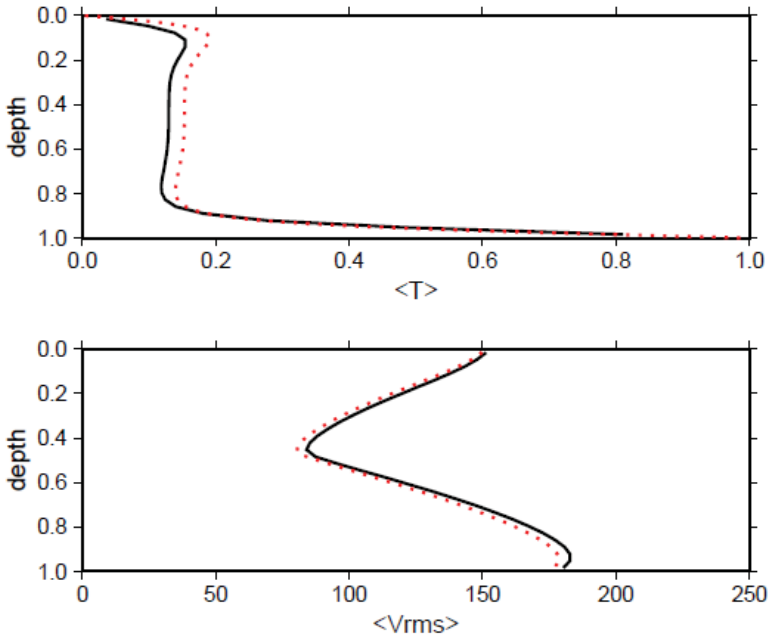

Figure 3.22: Average temperature and V_{RMS} with respect to depth of the shell of case C1. Results calculated from the radially-uniform grid in ASPECT are shown in black, and results calculated from CitcomS are shown in red dots.

significant shortening of runtime. To ensure that this is still a valid choice for the increased Rayleigh number convective flow of the C Family, the previously mentioned case is re-started with tolerance increased to the default, 10^{-7}. It was allowed to run for another 24 hours. Just like with the low A Family cases, the results are not significantly affected by the increased tolerance. Agreement is 3.58% for V_{RMS}, slightly better than the relaxed tolerance case, and -15.32% for average temperature, slightly worse than the relaxed tolerance case. No major shift is observed, so it is decided that the lower tolerance appears to still be valid.

One other check is run using C1 conditions. A few cases of A1 were run using an extremely small value of viscosity to get the desired $Ra = 7000$ rather than a large value of gravity. Mathematically, this should not affect the run, as the Rayleigh number is the same either way. The results are not significantly affected for the A1 cases, so a case of C1 using a small viscosity and gravity of 1 is performed to ensure there is still no major influence on the

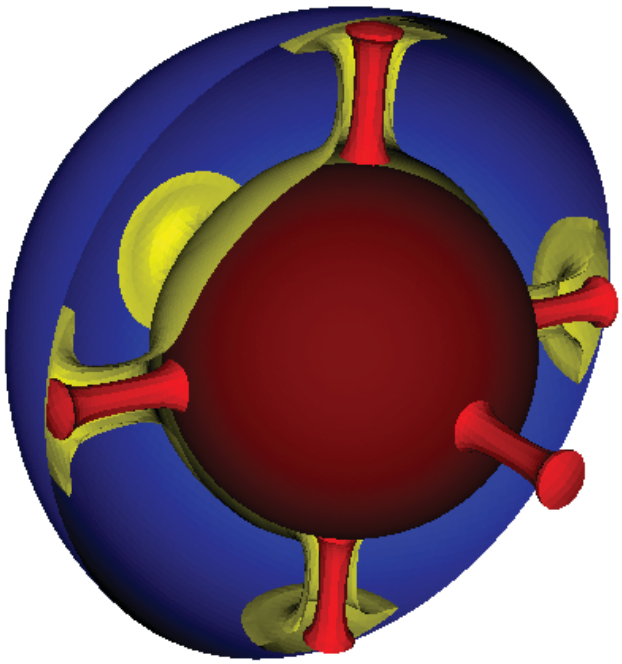

Figure 3.23: A series of isotherms generated from case C1 using a 12×32^3 radially-uniform grid. The dark red sphere represents the core, the bright red, thin tubes are the hot interiors of plumes of upwelling material, the yellow layer is colder, upwelling material, and the blue half-shell is the surface.

results. The case runs for almost exactly the same amount of time as the original and the results are not significantly changed. Agreement is 3.75% difference for V_{RMS} and -15.01% for average temperature. There is still no major change as long as the Rayleigh number is held constant, even for these higher Rayleigh number cases.

Case C2 is run on the radially-uniform grid at 12×32^3 resolution using a CFL number of 1.0 and the $D = 0.45$ geometry. The viscosity contrast, $\Delta\eta$, is 10 for this case, the same as case A2. It should be mentioned that this case uses the steady-state solution of case C1 as its initial conditions. The results are still fair to poor as compared to the benchmark, though they are in better agreement than C1. This case starts the noted trend that each C Family case is in better agreement than the previous. Agreement is 2.03% difference for

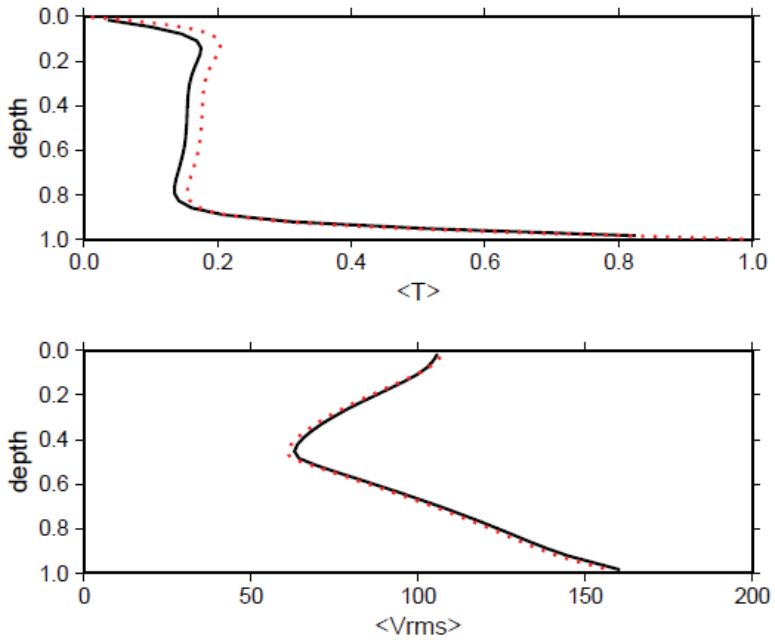

Figure 3.24: Average temperature and V_{RMS} with respect to depth of the shell of case C2. Results calculated from the radially-uniform grid in ASPECT are shown in black, and results calculated from CitcomS are shown in red dots.

V_{RMS} and -12.62% difference for average temperature. The planform is the standard six plume cubic (see Figure 3.23). Radial plots of runs of C2 using CitcomS and ASPECT show better agreement than case C1, however there is still a significant amount of offset, especially for average temperature (Figure 3.24). Once again, the general behavior of the two data sets between codes agree as seen in the shapes of the curves matching.

Case C3 is run on the radially-uniform grid at 12×32^3 resolution using a CFL number of 1.0 and the $D = 0.45$ geometry. The viscosity contrast, $\Delta\eta$, is 30 for this case, the same as case A3. Just like case C2, case C3 uses the steady-state solution of case C1 as its initial conditions. The results continue to improve in agreement to the benchmark from those of case C2, yet they are still only fair. Agreement is 1.83% difference for V_{RMS} and -10.97% difference for average temperature (Table 3.9). The planform is standard six plume cubic (see Figure 3.23. Radial plots between CitcomS and ASPECT again show general agreement in

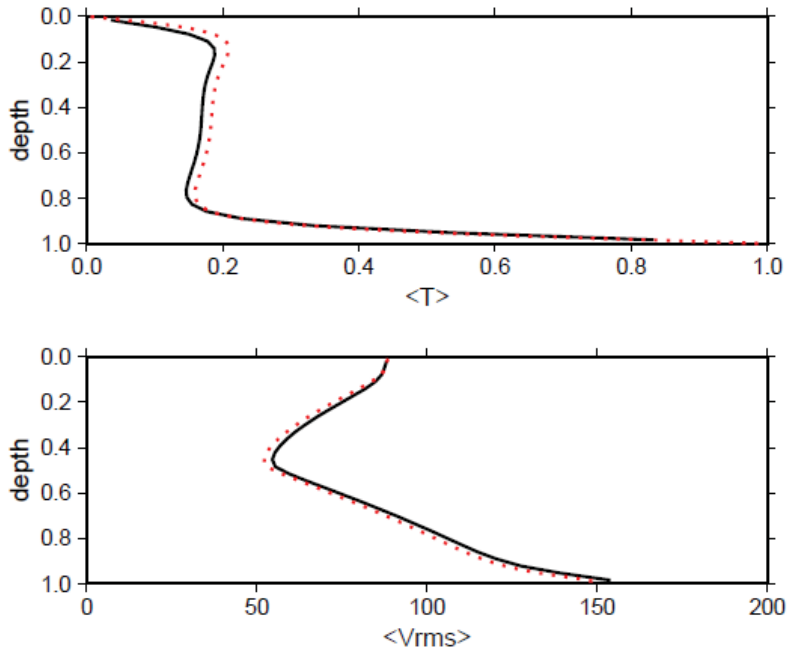

Figure 3.25: Average temperature and V_{RMS} with respect to depth of the shell of case C3. Results calculated from the radially-uniform grid in ASPECT are shown in black, and results calculated from CitcomS are shown in red dots.

behavior of both average temperature and V_{RMS}, but with a noticeable offset. The average temperature continues to have the most significant offset, though with each C Family case its agreement becomes better.

Case C4 is run on the radially-uniform grid at 12×32^3 resolution using a CFL number of 1.0 and the $D = 0.45$ geometry. The viscosity contrast, $\Delta\eta$, is 100 for this case, the same as case A4. For case C4, the steady-state solution of case C3 is used as the initial conditions. This means that case C4 requires the completion of case C3, which requires the completion of case C1, making case C4 the most computationally expensive run overall of all the cases tested. Results yet again improve from the previous case. Agreement is 1.47% difference for V_{RMS} and -8.27% difference for average temperature (Table 3.9), making case C4 the most well-agreed to Zhong et al. [35] of all the C Family cases. The planform is the standard six plume cubic (see Figure 3.23). This is an interesting result, as case C4 requires the

steady-state solutions of both case C3 and C1 as previously mentioned. Both case C1 and C3 have significant differences to the benchmark values, yet the results calculated for C4 are in better agreement than either.

All of the cases reported up to this point have not used adaptive mesh refinement, which ASPECT is designed to use by default. This is done to ensure a proper benchmark test between results reported in Zhong et al. [35] and results calculated here using ASPECT. However, the results calculated for the C Family have a bigger margin of error than expected. While it is not fully understood why the quadratic elements used by ASPECT would not function optimally without it, ASPECT is designed to run with both quadratic elements and adaptive mesh refinement. One last case of C1 is run using ASPECT at 12×32^3 refinement on the radially-uniform grid, but this time using the default settings of adaptive mesh refinement. Results calculated from this case are not in as good of agreement as was expected, however the result is significant. The V_{RMS} has a difference of 7.45% to the value for C1 reported in Zhong et al. [35]. This is about twice as high as the 12×32^3 case using the radially-uniform grid: 3.76%. The average temperature is the value most influenced by the adaptive mesh refinement, coming into about three times better agreement: -4.87% from the orignal -14.99% of the radially-uniform case. It should be noted that this value is in better agreement than the value calculated for average temperature for the radially-uniform grid at 12×64^3 refinement: -5.13%. The Nusselt number at the top of the shell has by far the largest difference from Zhong et al. [35], and it was hoped that adaptive mesh refinement would most help this term. This is not the case, as agreement got slightly better: -43.14% from -44.10%. The Nusselt number at the bottom of the shell got further from Zhong et al. [35] by a few percent: -12.27% from -9.04%. While these results are not as good as was expected, they do show a strong response to the activation of adaptive mesh refinement. How and when the mesh is adapted can be set in ASPECT, and it is possible that different

settings for the adaptive mesh refinement could produce results in closer agreement to Zhong et al. [35].

Chapter 4

Conclusions

In this study, I present spherical cases in both 2 and 3 dimensions. There are two main goals in doing this. The first is to test the new Geodynamics code ASPECT against results previously calculated by the legacy code CitcomS. The second is to benchmark the results calculated for the Zhong et al. [35] paper.

2D cases show good agreement to results reported in sections of the ASPECT manual and the studies these sections are based on. The 2D cases come from Blankenbach et al. [2], van Keken et al. [31], and Davies et al. (in preparation). Cases 1a through 1c as well as 2a are presented from Blankenbach et al. [2]. All four cases are in good agreement with Blankenbach et al. [2]. Case 2a has the farthest results from the paper, but still has a V_{RMS} within 0.005% and a Nusselt number within 0.002%. Behavior across cases is stable, but with small-scale oscillations still present in the final steady state time-evolution. Case 2a at 5 global refinements is the only exception, showing large-scale oscillations that do not damp down with time, but do average to acceptable values for both V_{RMS} and Nusselt number. Case 1a from van Keken et al. [31] is also presented. In this case, as well as the ASPECT manual, a smoothed boundary is used as opposed to the original discontinuous "stair-stepping" boundary presented in the paper. This test is in good agreement to the test in the ASPECT manual, with the final time-evolutions of both the V_{RMS} and the V_{MAX} converging completely. The final 2D case presented is case 2.1 from Davies et al. (in preparation). It too shows good agreement to the results in the ASPECT manual. The case

with 5 global refinements has the best agreement with 0.48% difference for V_{RMS} and 0.60% for average temperature.

3D cases are all based on Zhong et al. [35]. The cases tested are A1 through A8, or the "A Family," B1, and C1 through C4, or the "C Family." Cases in the A family and B1 show generally good agreement, while cases in the C Family show fair agreement. In terms of shape and magnitude of convective flow, all cases perform as expected. All cases are run using a grid with uniform element spacing in the radial direction. This is done to make the grid more like that of CitcomS, which has constant grid element sizes. All cases are run at global refinement 5, corresponding to a grid of 12×32^3 cells. Values are calculated for average V_{RMS}, average temperature, and the Nusselt numbers for the top and bottom of the shell. Results for V_{RMS} and average temperature for cases A1 through A6 agree to within 3.0% with most cases agreeing to within 1.0%. Case A7 agrees to within 3.0% for V_{RMS} and 2.0% for average temperature. Case A8 agrees to about 11.2% for V_{RMS} and 4.0% for average temperature. Case B1 has similar agreement to A1, with V_{RMS} agreeing to within 1.0% and average temperature to within 3.0%. Cases C1 through C4 have worse agreement, with V_{RMS} agreeing to within 4.0% and average temperature to within 15.0%. With respect to the C Family from C1 to C4, agreement improves to within 1.5% and 8.5%, respectively. Cases A1 and C1 are rerun using global refinement 6, corresponding to a grid of 12×64^3 cells. Agreement to Zhong et al. [35] is increased significantly in both cases. Case A1 agrees to within 0.1% for V_{RMS} and 0.9% for average temperature. Case C1 agrees to within 0.6% for V_{RMS} and 5.2% for average temperature. Results for the Nusselt numbers tend to be in worse agreement. Nusselt numbers at the bottom of the shell are in better agreement than Nusselt numbers at the top, with several cases having different Nusselt numbers at the top and bottom. Cases A1, A3, and A7 are chosen to be run on different grids and at various global refinements. They are chosen because A1 is isoviscous, A3 is low viscosity contrast,

and A7 is high viscosity contrast. Cases A1 and A3 are in an active lid regime, while A7 is in a stagnant lid regime. The grids tested are the uniformly spaced radial grid used in each case, versus a grid where the cells get smaller as you move inward radially. The latter grid is the default setup for ASPECT. It is hypothesized that cases in stagnant lid regime will be better resolved using a grid with radially varying cells, as they will be more refined internally to better calculate the more complex flow. Cases A1 and A3 have the best agreement using a grid with cells spaced uniformly, while A7 has the best agreement using a grid with cells that has varying radial spacing.

While results calculated with ASPECT are generally good, they are often not as good as expected. There are several reasons why this could be. One potential detail is that ASPECT is designed to use both quadratic elements and adaptive mesh refinement, as well as use a mesh that has cells that change spacing with radius. For these cases, adaptive mesh refinement is turned off and the mesh held constant in the radial direction. It is possible that the quadratic elements are most effective with adaptive mesh refinement turned on.

The cases of A1, A3, and A7 run at various refinements serve to demonstrate how the solution of each case is changing with refinement. In log-log space, it is expected that solutions converging linearly will produce a slope of 1, while solutions converging quadratically will have a slope of 2. While the cases using the ASPECT default grid, indeed, have steeper slopes to their data points, they are not as steep as expected. Note the extrapolated values used to normalize the results are calculated using different grids. The CitcomS extrapolated values are calculated from runs using grids at 12×32^3, 12×64^3, and 12×96^3 refinement, accept for case A7 which uses 12×16^3, 12×32^3, and 12×64^3. The ASPECT extrapolated values are calculated from runs using grids at 12×8^3, 12×16^3, and 12×32^3 refinement, accept for case A1 which uses 12×16^3, 12×32^3, and 12×64^3. The quadratic element grids ASPECT uses are more computationally expensive, and therefore higher refinement runs are

not run for cases A3 and A7. It now appears that higher refinement than expected is needed even with quadratic elements. Due to this effect, it is possible the extrapolated values for ASPECT will improve significantly with finer grids.

Nusselt numbers tend to be in worse agreement than either V_{RMS} or average temperature for each case tested. There is also discrepancy in the values of the Nusselt numbers from the top and bottom of the same case. It is noted that increasing the resolution increases the agreement while decreasing the discrepancy. While this is a seemingly trivial result, the fact that ASPECT uses quadratic elements by default implies that differences of Nusselt numbers from the same grid of this magnitude should only occur on coarse grids. This is because, theoretically, a coarser grid using quadratic elements should have a similar resolution to a finer grid using linear elements. In order to bring Nusselt numbers to similar values a surprising amount of refinement is needed. The 2D results calculated from Blankenbach et al. [2] and Davies et al. (in preparation) support this idea, with higher refinements needed to bring values for the V_{RMS} and Nusselt numbers into agreement.

Another potential fix for the Nusselt numbers is how they are calculated. ASPECT outputs data for both heat flux as well as heat flux density, that is, the heat flux with respect to the surface area of the boundary it is flowing through. From there, the Nusselt numbers are calculated using the inner and outer radii, and Equations 35 and 36 given in Zhong et al. [35], where Q_t and Q_b are the heat flux densities through the top and bottom layers, respectively. There are two possible ways ASPECT could calculate the heat flux densities through the top and bottom boundaries: using the temperature gradient along the surfaces of the boundaries or the temperature gradient through the whole volume of the cells of the surfaces. While both are viable methods to calculate heat flux densities, testing has shown that using the whole volume produces better results. ASPECT currently calculates heat flux densities using the gradient along the surface. It is possible that switching this calculating

scheme can produce better Nusselt numbers.

ASPECT is still a new geodynamics code that continues to improve and evolve. Scientists from all over the world have contributed to its improvement and the community continues to grow. During this work, the ability to change the solver scheme from the default equations in ASPECT to equations following the Boussinesq approximation, as well as ALA and TALA, was added to the ASPECT code. This change alone significantly improved the results of this work. These cases are all designed to run as similarly to how they would be run in CitcomS for the purpose of benchmarking. However, ASPECT is designed to run using adaptive mesh refinement, and while initial results here are not as good as expected there is still more work to be done in the future. It has been shown that adaptive mesh refinement does have a significant effect on the calculated results, and how the mesh adapts as well as how often it adapts can both be adjusted.

Bibliography

[1] D. Bercovici, Y. Ricard, and M. Richards. The relationship between mantle dynamics and plate tectonics: a primer. In M. Richards, R. Gordon, and R. D. van der Hilst, editors, *The History and Dynamics of Global Plate Motions*, volume 121 of *Geophys. Monograph*, pages 5–46. American Geophysical Union, Washington, DC, 2000.

[2] B. Blankenbach, F. Busse, U. Christensen, L. Cserepes, D. Gunkel, U. Hansen, H. Harder, G. Jarvis, M. Koch, G. Marquart, D. Moore, P. Olson, H. Schmeling, and T. Schnaubelt. A benchmark comparison for mantle convection codes. *Geophys. J. Int.*, 98:23–38, 1989.

[3] U. R. Christensen and D. A. Yuen. The interaction of a subducting lithospheric slab with a chemical or phase boundary. *J. Geophys. Res.*, 89:4389–4402, 1984.

[4] G. F. Davies. Role of the lithosphere in mantle convection. *J. Geophys. Res.*, 93: 10451–10466, 1988.

[5] G. F. Davies. Mantle convection with a dynamic plate: topography, heat flow and gravity anomalies. *Geophys. J.*, 98:461–464, 1989.

[6] C. DeMets, R. G. Gordon, D. F. Argus, and S. Stein. Current plate motions. *Geophys. J. Int.*, 101:425–478, 1990.

[7] R. S. Dietz. Continent and ocean evolution by spreading of the sea floor. *Nature*, 190: 854–857, 1961.

[8] D. W. Forsyth and S. Uyeda. On the relative importance of the driving forces of plate motion. *Geophys. J. R. Astr. Soc.*, 43:163–200, 1975.

[9] C. W. Gable. *Numerical Models of Plate Tectonics and Mantle Convection in Three Dimensions*. PhD thesis, Harvard University, Cambridge MA, 1989.

[10] G. T. Jarvis and D. P. McKenzie. Convection in a compressible fluid with infinite prandtl number. *Journal of Fluid Mechanics*, 96:515–583, 1980. doi: 10.1017/S002211208000225X.

[11] G. T. Jarvis and W. R. Peltier. Convection models and geophysical observations. In W. R. Peltier, editor, *Mantle convection: Plate Tectonics and Global Dynamics*, volume 4 of *The Fluid Mechanics of Astrophysics and Geophysics*, pages 479–593. Gordon and Breach Science Publishers, New York, NY, 1989.

[12] S. D. King. On topography and geoid from 2-d stagnant lid convection calculations. *Geochem., Geophys., Geosys.*, 10(Q03002), 2009. doi: 10.1029/2008GC002250.

[13] S. D. King and B. H. Hager. The relationship between plate velocity and trench viscosity in Newtonian and power-law subduction calculations. *Geophys. Res. Lett.*, 17:2409–2412, 1990.

[14] S. D. King and J. Ritsema. African hot spot volcanism: Small-scale convection in the upper mantle beneath cratons. *Science*, 290:1137–1140, 2000.

[15] S. D. King, D. A. Raefsky, and B. H. Hager. ConMan: vectorizing a finite element code for incompressible two-dimensional convection in the Earth's mantle. *Phys. Earth Planet. Inter.*, 59:195–207, 1990.

[16] S. D. King, C. Lee, P. E. Van Keken, W. Leng, S. Zhong, E. Tan, N. Tosi, and M. C. Kameyama. A community benchmark for 2-d cartesian compressible convection in the earth's mantle. *Geophys. J. Int.*, 180:73–87, 2010. doi: 10.1111/j.1365-246X.2009.04413.x.

[17] Martin Kronbichler, Timo Heister, and Wolfgang Bangerth. High accuracy mantle convection simulation through modern numerical methods. *Geophysics Journal International*, 191:12–29, 2012.

[18] L. N. Moresi and V. S. Solomatov. Numerical investigations of 2D convection with extremely large viscosity variations. *Phys. Fluids*, 7:2154–2162, 1995.

[19] L. N. Moresi, S. Zhong, and M. Gurnis. The accuracy of finite element solutions of stokes's flow with strongly varying viscosity. *Phys. Earth Planet. Inter.*, 97:83–94, 1996.

[20] W. J. Morgan. Rises, trenches, great faults, and crustal blocks. *J. Geophys. Res.*, 73: 1959–1982, 1968.

[21] L. Noack and D. Breuer. First- and second-order frank-kamenetskii approximation applied to temperature-, pressure- and stress- dependent rheology. *Geophys. J. Int.*, 195:27–46, 2013.

[22] J. T. Ratcliff, G. Schubert, and A. Zebib. Steady tetrahedral and cubic patterns of spherical- shell convection with temperature-dependent viscosity. *J. Geophys. Res.*, 101:25473–25484, 1996.

[23] B. Schmandt and E. Humphreys. Complex subduction and small-scale convection revealed by body-wave tomography of the western United States upper mantle. *Earth Planet. Sci. Lett.*, 297:435–445, 2010.

[24] G. Schubert, D. L. Turcotte, and P. Olson. *Mantle Convection in the Earth and Planets*. Cambridge University Press, 2001.

[25] N. Sleep. Plate tectonics through time. In G. Schubert, editor, *Treatise on Geophysics*, volume 9, pages 145–169. Elsevier, Amsterdam, 2007.

[26] K. Stemmer, H. Harder, and U. Hansen. A new method to simulate convection with strongly temperature-dependent and pressure-dependent viscosity in a spherical shell: Applications to the earth's mantle. *Phys. Earth Planet. Inter.*, 157:223–249, 2006.

[27] P. J. Tackley. Mantle convection and plate tectonics: Toward an integrated physical and chemical theory. *Science*, 288:2002–2007, 2000.

[28] E. Tan, E. Choi, P. Thoutireddy, M. Gurnis, and M. Aivazis. GeoFramework: Coupling multiple models of mantle convection within a computational framework. *Geochem., Geophys., Geosys.*, 7, 2006. doi: 10.1029/2005GC001155.

[29] D. L. Turcotte and E. R. Oxburgh. Finite amplitude convective cells and continental drift. *J. Fluid Mech.*, 28:29–42, 1967.

[30] D. L. Turcotte and G. Schubert. *Geodynamics*. Cambridge University Press, Cambridge, 2 edition, 2002.

[31] P. E. van Keken, S. King, H. Schmeling, U. Christensen, D. Neumeister, and M.-P. Doin. A comparison of methods for the modeling of thermochemical convection. *J. Geophys. Res.*, 102:22477–22495, 1997.

[32] M. Yoshida and A. Kageyama. Application of the yin-yang grid to a thermal convection of a boussinesq fluid with infinite prandtl number in a three-dimensional spherical shell. *Geophys. Res. Lett.*, 31(L12609), 2004. doi: 10.1029/2004GL019970.

[33] S. Zhong and M. Gurnis. Controls on trench topography from dynamic models of subducted slabs. *J. Geophys. Res.*, 99:15683–15695, 1994.

[34] S. Zhong, M. T. Zuber, L. Moresi, and M. Gurnis. Role of temperature-dependent viscosity and surface plates in spherical shell models of mantle convection. *J. Geophys. Res.*, 105:11063–11082, 2000.

[35] S. Zhong, A. McNamara, E. Tan, L. Moresi, and M. Gurnis. A benchmark study on mantle convection in a 3-d spherical shell using citcoms. *Geochem., Geophys., Geosys.*, 9, 2008. doi: 10.1029/2008GC002048.